

## Multiscale Momentum Flux and Diffusion due to Whitecapping in Wave–Current Interactions

JUAN M. RESTREPO

*Department of Mathematics, Department of Atmospheric Sciences, and Physics Department,  
The University of Arizona, Tucson, Arizona*

JORGE M. RAMÍREZ

*Universidad Nacional de Colombia, Sede Medellín, Escuela de Matemáticas, Medellín, Colombia*

JAMES C. MCWILLIAMS

*Department of Atmospheric and Oceanic Sciences, University of California, Los Angeles, Los Angeles, California*

MICHAEL BANNER

*School of Mathematics and Statistics, University of New South Wales, Sydney, New South Wales, Australia*

(Manuscript received 12 June 2009, in final form 5 May 2010)

### ABSTRACT

Whitecapping affects the Reynolds stresses near the ocean surface. A model for the conservative dynamics of waves and currents is modified to include the averaged effect of multiple, short-lived, and random wave-breaking events on large spatiotemporal scales. In this study's treatment, whitecapping is parameterized stochastically as an additive uncertainty in the fluid velocity. It is coupled to the Stokes drift as well as to the current velocity in the form of nonlinear momentum terms in the vortex force and the Bernoulli head. The effects of whitecapping on tracer dynamics, mass balances, and boundary conditions are also derived here. Whitecapping also modifies the dynamics and the size of the sea surface boundary layer. This study does not resolve the boundary layer, however, the authors appeal to traditional viscosity parameterizations to include these diffusive effects, modified for the context of wave–current interactions.

The parameterized breaking velocity field is endowed with empirical rules that link their generation in space and time to properties and dynamics of wave groups. The energy convergence rate of wave groups is used as an indicator for the onset of wave breaking. A methodology is proposed for evaluating this criterion over an evolving random Gaussian model for the ocean surface. The expected spatiotemporal statistics of the breaking events are not imposed, but rather computed, and are found to agree with the general expectation of its Poisson character. The authors also compute, rather than impose, the shear stress associated with the breaking events and find it to agree with theoretical expectations.

When the relative role played by waves and breaking events on currents is compared, this study finds that waves, via the vortex force, purely advect the vorticity of currents that are essentially only dependent on transverse coordinates. The authors show that currents will tend to get rougher in the direction of steady wind, when whitecapping is present. Breaking events can alter and even suppress the rate of advection in the vortex force. When comparing the rates of transport, the waves will tend to dominate the short term and the whitecapping of the long-term rate.

---

### 1. Introduction

After the wind has been acting on the ocean surface for some time, the amplitude of the fastest growing wave component can reach a critical unstable steepness for

---

*Corresponding author address:* J. M. Restrepo, Dept. of Mathematics, The University of Arizona, Tucson, AZ 85721.  
E-mail: restrepo@physics.arizona.edu

which whitecapping occurs (for details and references see Banner and Peregrine 1993). We refer to the process of steepening, whitecapping, and changing amplitude as *wave breaking*. These short-lived, spatiotemporally random events reduce the excess energy in the wave field and modify the momentum of the background currents locally (see Melsom 1996). The dissipation sometimes changes dramatically when a sudden change in wind strength and/or wind direction occurs. In addition to dissipative effects, Melville (1996) recounts in his review the extent to which we know how wave-breaking events modify the dynamics of the currents: they affect the Reynolds stresses and they entrain air bubbles in the upper layer of these currents. Breaking waves are especially important in enhancing the wind–sea coupling (see Terray et al. 1996) and turbulence production at the surface (see Gemmrich and Farmer 2004). The connection between wave breaking and near-surface turbulence is natural and has been considered at some length by Craig and Banner (1994) and Burchard (2001).

Whitecapping also affects the thickness of the mixed layer, making boundary layer effects on the currents more prominent (cf. D’Asaro 2001). Observations suggest that breaking waves make a large contribution to mixed layer turbulence levels in the surface layer. For very shallow mixed layers less than  $O(10\text{ m})$  deep, wave breaking plays an important and direct role in mixed layer deepening. For intermediate depth layers, the most important contribution of wind–wave forcing consists of driving the mean motion of the mixed layer and thus the shear at the mixed layer base. For deeper layers, surface cooling and convection probably dominate, with wind and breaking waves keeping the upper mixed layer well stirred.

The inclusion of breaking effects in ocean dynamics models is often essential. At present, however, we have only a partial understanding of how wave breaking affects the basic flow quantities, such as velocities and stresses. Wave breaking has no complete theory yet, and its modeling is accomplished via parameterizations, some of which can be very sophisticated (Bauer et al. 1988; Alves and Banner 2003; Komen et al. 1994; see also Warner and McIntyre 1999 and references therein).

Our focus here is on the large-scale dynamics of the wave-driven ocean circulation at shelf to basin scales; scales far greater than those typical of the waves and whitecapping events. The three-dimensional and time-dependent conservative dynamics of waves and currents at these scales have been elaborated in McWilliams and Restrepo (1999) and more completely in McWilliams et al. (2004). A comparison between this “vortex force” model and the “radiation stress” formulation for waves and currents of Hasselmann and others appears in Lane et al. (2007).

How whitecapping affects wave–current interactions was addressed, to some extent, within the same framework in Restrepo (2007). There, the proposed parametric representation of breaking as a diffusion term represents added uncertainty to a Lagrangian-frame representation of fluid parcel dynamics. The resulting Langevin-like stochastic differential equations for fluid parcel motions were then phase averaged and projected onto the Eulerian frame. The result was a wave–current interaction model with attendant boundary conditions that took into account velocity uncertainties.

The fact that noise, modeled as a stochastic process, can be related to dynamic dissipation at macroscopic scales is one of the most common yet profound notions of theoretical physics of collective phenomena. The Lagrangian perspective is, in our opinion, a natural setting in which to develop an appropriate drift–diffusion model for parcel dynamics with surface breaking. However, we revert here to an Eulerian perspective to revisit wave–current interaction, with added wave-breaking effects. In contrast to the strong-noise limit and Lagrangian-based approach of Restrepo (2007), we will use Gaussian random wave fields and current knowledge of the kinematics of individual breaking events to arrive at an Eulerian-averaged effect of wave breaking on currents. Eventually we will make the Lagrangian- and Eulerian-frame characterization of the phenomenology physically consistent and equivalent.

In addition to this, we also develop a computational procedure for capturing key aspects of the relationship between wave group dynamics and breaking. (see the introduction in Tian et al. 2008 as well as Alves and Banner 2003 for details on the kinematics of wave breaking). Specifically, we incorporate the wave group energy convergence rate and use it as a breaking initiation threshold (see Banner and Peirson 2007 and Song and Banner 2002). Furthermore, we extend the techniques of wave group detection and wave group analysis, pioneered by Longuet-Higgins (1984) and further developed by Song and Banner (2002), to the two-dimensional case. Along the way, we also propose the *mean Euler characteristic* as an important parameter in the identification of wave groups in random wave fields.

In some aspects, the model presented here is reminiscent of recent work on whitecapping effects to the mixed layer, near the sea ocean surface, by Sullivan and collaborators (see Sullivan et al. 2007 and references therein); we treat breaking events as impulsive stochastic elements, and we treat the dissipative role of breaking in the very same way as they did in their work. However, in addition to focusing on the role played by wave breaking in the net momentum fluxes in wave–current interactions and sea surface conditions, we derive the statistical

distribution of breaking events and predict the mean momentum flux due to breaking. These two are imposed in the strategy proposed by Sullivan and collaborators. Though not crucial to our results owing to our interest in vastly larger spatiotemporal scales, we also adopt an analytical parameterization of individual breakers, which they obtained from fitting laboratory data. In the work of Sullivan et al., the impulsive breakers are added to the momentum equation. Based upon arguments presented in Restrepo (2007), we instead propose that the impulsive breakers appear as an additive uncertainty effect in the velocity.

### 2. Large-scale wave current and whitecapping dynamics

Our goal is to use the very same machinery used in McWilliams and Restrepo (1999) to derive a consistent representation for waves and currents and to derive how the vortex force and the Bernoulli head are modified by the presence of an additive stochastic component because of wave breaking. For expository reasons we will not be using the more complete wave–current dynamics developed in McWilliams et al. (2004), opting instead for the derivation in McWilliams and Restrepo (1999). The result is a far simpler wave–current interaction description, appropriate for planetary-scale quasigeostrophic scales and dynamics, which do not include effects of currents on waves or higher-order rotational effects due to waves.

Considered here is an oceanic region on the rotating earth containing a stratified, incompressible fluid, whose upper free surface is at  $z = \eta(\mathbf{x}, t)$ , and whose rigid lower boundary is at  $z = -H(x)$ . The vertical coordinate that is aligned antiparallel to the local gravitational force and is denoted by  $z$ ,  $z = 0$  corresponds to a quiescent ocean surface;  $\hat{\mathbf{z}}$  will denote the unit upward-pointing vector. The position vector is denoted by  $(\mathbf{x}, z)$ , where the transverse or horizontal component is  $\mathbf{x}_h = (x, y)$ . A time typical of the wave scales and breaking is denoted by  $t$ . A longer time scale  $T = \varepsilon^2 t$  is typical of the changes in the currents velocity field (the  $\varepsilon \ll 1$  can be justified in terms of the ratio between wave time scales  $\omega^{-1}$  and the time scales in which changes in wind forcing appreciably affect the currents). Here,  $\omega$  is the gravity wave peak frequency.

The transverse component of differential operators and vector variables has a subscript  $h$ ; for example,

$$\nabla \equiv \left( \nabla_h, \frac{\partial}{\partial z} \right) \quad \text{and} \quad \frac{D}{Dt} = \frac{\partial}{\partial t} + q_h \cdot \nabla_h + \omega \frac{\partial}{\partial z}.$$

The oceanic dynamics are represented, as in Craik and Leibovich (1976), by the Boussinesq momentum and continuity equations,

$$\mathbf{q}_t + (\mathbf{q} \cdot \nabla)\mathbf{q} + 2\boldsymbol{\Omega} \times \mathbf{q} - \vartheta \hat{\mathbf{z}} + \frac{1}{\rho_0} \nabla \tilde{p} = \nabla \cdot \mathbf{R}^c, \quad \nabla \cdot \mathbf{q} = 0, \tag{1}$$

where  $\mathbf{R}^c$  is a stress tensor,  $g$  is the gravitational acceleration, and  $\rho$  is the density, with  $\rho_0$  its mean value;  $\mathbf{q}$  is the Eulerian velocity. The buoyancy field is defined by  $\tilde{\vartheta} = g(1 - \rho/\rho_0)$ , where the dynamic pressure  $\tilde{p}$  does not include the hydrostatic contribution  $p_{\text{atm}} - g\rho_0 z$  due to the mean atmospheric surface pressure  $p_{\text{atm}}$  and the mean density of the resting ocean. The projection of the Coriolis vector, directed along the earth’s axis of rotation, onto the local Cartesian coordinate system is  $2\boldsymbol{\Omega} = (0, f^{(y)}(y), f^{(z)}(y))$ , the superscripts indicating the components. Its spatial dependence is a consequence of variations of the local vertical direction with latitude. Since energetic, extratropical atmospheric and oceanic motions typically have large horizontal scales in comparison to the thickness of the fluid layer itself, it is usually possible to neglect the  $y$  component of the Coriolis vector.

We shall assume, for simplicity, that the buoyancy depends linearly on one or more passive tracers  $\tilde{\theta}(\mathbf{x}_h, z, t)$ , such as temperature or salinity, instead of the true nonlinear equation of state for seawater. The equation of state may thus be written as

$$\tilde{\vartheta} = g \sum_{\theta} \mu \tilde{\theta}, \tag{2}$$

where  $\mu$  is the expansion coefficient for  $\tilde{\theta}$ , and  $\sum_{\theta}$  denotes the sum over all the tracers that contribute to the buoyancy. In turn, the tracer dynamics are given by

$$\frac{D\tilde{\theta}}{Dt} = Q(\tilde{\theta}), \tag{3}$$

where  $Q$  is the tracer diffusion term. We further assume that the tracer and buoyancy fields have a mean vertical stratification in the absence of any motion. Thus, we write the total buoyancy field as

$$\tilde{\vartheta} = \int^z N^2(z') dz' + \vartheta^*(\mathbf{x}, t), \tag{4}$$

where  $N(z)$  is the Brünt–Väisälä frequency of the mean buoyancy stratification, and  $\vartheta^*$  is the buoyancy deviation associated with fluid motions. Accompanying the mean stratification are each of the mean vertical tracer profiles  $\Theta(z)$ , so that

$$\tilde{\theta} = \Theta(z) + \theta^*(\mathbf{x}, t).$$

The pressure  $\tilde{p}$  is assumed to have a mean  $\Pi(z)$  and deviation  $p^*$ . The mean pressure is in hydrostatic balance

with the mean stratification (see McWilliams and Restrepo 1999). The surface boundary conditions at  $z = \eta(\mathbf{x}_h, t)$  are as follows:

$$\begin{aligned} \omega &= \frac{D\eta}{Dt}, \quad \tilde{p} = g\rho_0\eta + \tilde{p}_{\text{atm}}, \quad \nu \frac{\partial \mathbf{q}}{\partial z} = \frac{1}{\rho_0} \boldsymbol{\tau}, \quad \text{and} \\ k \frac{\partial \tilde{\theta}}{\partial z} &= \mathcal{T}, \end{aligned} \quad (5)$$

where  $\boldsymbol{\tau}$  and  $\mathcal{T}$  are the wind stress and surface tracer flux, respectively.

We are concerned with the situation whereby currents are influenced by surface gravity waves, characterized by wave groups of typical amplitude  $a$  and mean horizontal wavenumber with magnitude  $k = |\mathbf{k}|$ . We assume that the wave slope  $\varepsilon = ka$  is a small number and that  $k|D| \gg 1$  (where  $D$  is the typical depth), so that these wave groups, to leading order, are approximately linear and uninfluenced by the ocean bottom. These assumptions lead to the deep-water dispersion relation  $\sigma = \sqrt{gk}$ , where  $\sigma$  is the frequency.

We nondimensionalize (1)–(5) by characteristic wave-propagation scales, that is, by the time scale  $1/\sigma_0$  and the space scale  $1/k_0$ . The corresponding velocity scale is  $\sigma_0/k_0$ , the pressure scale is  $\rho_0(\sigma_0/k_0)^2$ , the buoyancy scale is  $\sigma_0^2/k_0 \times B_0$ , and the tracer scale is  $\sigma_0^2/(k_0 g \mu) \times B_0$ . The surface elevation  $\eta$  is scaled by  $1/k_0$ . In addition, we designate the Coriolis scale by  $\sigma_0 \times \Omega_0$ . The Coriolis value is  $\Omega_0$ . The Brünt–Väisälä scale by  $\sigma_0 \times N_0$ , the viscosity and tracer diffusivity scale by  $\sigma_0/k_0^2 \times \nu_0$ , the wind stress scale by  $\rho_0(\sigma_0/k_0)^2 \times \tau_0$ , and the tracer flux scale by  $\sigma_0^3/(k_0^2 g \mu) \times \mathcal{T}_0$ . The nondimensional values of the  $B_0$ ,  $\Omega_0$ ,  $N_0$ ,  $\nu_0$ ,  $\tau_0$ , and  $\mathcal{T}_0$  will be chosen to preserve certain balances in the asymptotic theory. We seek a general form for the asymptotic theory; that is, we choose values of the expansion parameters that allow all the various terms to enter together at the leading nontrivial order in the governing equations for the evolution of the vorticity  $\boldsymbol{\omega}$  on the slow time scale. The relations among the nondimensional parameters that allow this are the following:

$$\Omega_0, \|\mathbf{R}\|, N_0, \nu_0 = O(\varepsilon^2); \quad B_0, \tau_0, \mathcal{T}_0 = O(\varepsilon^4). \quad (6)$$

Later we shall be more specific about the size of these parameters in the physical setting.

The three-dimensional velocity field  $\mathbf{q} := (\mathbf{q}_h, w^q)$  is decomposed into an irrotational wave-associated velocity, currents, and a breaking velocity field:

$$\mathbf{q}(\mathbf{x}, t, T) = \varepsilon \mathbf{u}^w(\mathbf{x}, t) + \varepsilon^2 \mathbf{v}^c(\mathbf{x}, t, T) + \varepsilon^2 \mathbf{b}(\mathbf{x}, t, T). \quad (7)$$

We will use the convention to overload the definition of a velocity vector  $v := (\mathbf{v}_h, w^p)$ , with  $\mathbf{v}$  representing the “wave” velocity  $\mathbf{u}^w$ , the “current” velocity  $\mathbf{v}^c$ , or the “breaking” velocity  $\mathbf{b}$ .

In the following, we work out the two main contributions of wave breaking the dynamics of waves and currents: the modification of the momentum equations due to Reynolds-like stresses, which we denote as *breaking-generated momentum flux* and the enhancement of surface boundary layer effects. The enhanced diffusivity due to the change in the boundary layer thickness owing to the presence of whitecapping we denote as the *breaking-generated diffusion*.

#### a. The breaking-generated momentum flux

Since the wave velocity field is assumed irrotational, the total vorticity is given by

$$\nabla \times \mathbf{q} = \varepsilon^2 (\nabla \times \mathbf{v}^c + \nabla \times \mathbf{b}) = \varepsilon^2 (\boldsymbol{\omega}_0 + \varepsilon \boldsymbol{\omega}_1 + \dots) = \varepsilon^2 \boldsymbol{\omega}. \quad (8)$$

The nondimensional vorticity equation thus reads

$$\begin{aligned} \frac{\partial \boldsymbol{\omega}}{\partial t} + \varepsilon^2 \frac{\partial \boldsymbol{\omega}}{\partial T} &= \nabla \times [(\varepsilon \mathbf{u}^w + \varepsilon^2 \mathbf{v}^c + \varepsilon^2 \mathbf{b}) \\ &\quad \times (\boldsymbol{\omega}_0 + \varepsilon \boldsymbol{\omega}_1 + \varepsilon^2 \boldsymbol{\omega}_2 + \dots + 2\boldsymbol{\Omega})] \\ &\quad + \varepsilon^2 \nabla \times (\nabla \cdot \mathbf{R}^c) + \varepsilon^2 \nabla \times \hat{\mathbf{z}} [\varepsilon^2 \theta + \theta^w]. \end{aligned} \quad (9)$$

The stress term  $\mathbf{R}^c$  is associated with wave-breaking diffusion. The details of this term will be worked out subsequently.

The nondimensional (tracer and) buoyancy equation becomes

$$\begin{aligned} \frac{\partial \theta}{\partial t} + \varepsilon^2 \frac{\partial \theta}{\partial T} &+ [\varepsilon \mathbf{u}^w + \varepsilon^2 \mathbf{v}^c + \varepsilon^2 \mathbf{b}] \cdot \nabla [\varepsilon^2 \theta + \theta^w] + \varepsilon^2 N^2 w \\ &= \varepsilon^2 Q(\theta), \end{aligned} \quad (10)$$

where  $Q$  is the breaking-generated diffusion term associated with (tracers and) buoyancy. Here,  $\theta^w$  is the additive portion of  $\theta$  associated with wave-scale dynamics.

The zero-order vorticity satisfies

$$\frac{\partial \boldsymbol{\omega}_0}{\partial t} = 0. \quad (11)$$

To first order, (9) gives

$$\frac{\partial \boldsymbol{\omega}_1}{\partial t} = \nabla \times [\mathbf{u}^w \times \boldsymbol{\omega}_0]. \quad (12)$$

Upon integration over small time scales,

$$\boldsymbol{\omega}_1(\cdot, t) = \nabla \times [\mathbf{U}^w \times \boldsymbol{\omega}_0], \quad \mathbf{U}^w(\cdot, t) := \int_0^t \mathbf{u}^w(\cdot, s) ds. \quad (13)$$

To second order,

$$\begin{aligned} \frac{\partial \boldsymbol{\omega}_0}{\partial T} = & \nabla \times (\mathbf{V}^c + \mathbf{Z}^c) + \nabla \times [\mathbf{V} \cdot \mathbf{R}^c(\mathbf{v}^c, \mathbf{b})] \\ & + \nabla \times (\mathbf{b} \times \mathbf{Z}^c) + \nabla \times [\mathbf{b} \times (\mathbf{V} \times \mathbf{b})] + \nabla \\ & \times [\mathbf{V}^c \times (\mathbf{V} \times \mathbf{b})] + \nabla \times \hat{\mathbf{z}}\theta, \end{aligned} \quad (14)$$

where

$$\mathbf{V}^c = \mathbf{v}^c + \mathbf{u}^{\text{St}}, \quad \mathbf{Z}^c = \nabla \times \mathbf{v}^c + 2\boldsymbol{\Omega}. \quad (15)$$

The current velocity equations are thus

$$\begin{aligned} \frac{\partial}{\partial T}(\mathbf{v}^c + \mathbf{b}) = & \mathbf{V}^c \times \mathbf{Z}^c + (\mathbf{b} \times \mathbf{Z}^c) + [\mathbf{b} \times (\mathbf{V} \times \mathbf{b})] \\ & + [\mathbf{V}^c \times (\mathbf{V} \times \mathbf{b})] - \nabla \Phi^c - \frac{1}{2} \nabla |\mathbf{b}|^2 \\ & + \hat{\mathbf{z}}\theta + \nabla \cdot \mathbf{R}^c(\mathbf{v}^c, \mathbf{b}), \end{aligned} \quad (16)$$

where the geopotential  $\Phi^c$  is given by

$$\Phi^c = p_0 + \frac{1}{2} |\mathbf{V}^c|^2. \quad (17)$$

Taking ensemble average and time averages gives

$$\begin{aligned} \frac{\partial \mathbf{v}^c}{\partial T} = & \mathbf{V}^c \times \mathbf{Z}^c + (\mathbf{B} \times \mathbf{Z}^c) + \langle \mathbf{b} \times (\mathbf{V} \times \mathbf{b}) \rangle \\ & + [\mathbf{V}^c \times \langle \mathbf{V} \times \mathbf{b} \rangle] - \nabla \Phi^c - \frac{1}{2} \langle \nabla |\mathbf{b}|^2 \rangle \\ & + \hat{\mathbf{z}}\theta + \langle \nabla \cdot \mathbf{R}^c(\mathbf{v}^c, \mathbf{b}) \rangle. \end{aligned} \quad (18)$$

The ensemble average  $\langle \cdot \rangle$  is taken with respect to the measure describing the random distribution of the breaking events. The time average  $\bar{\cdot}$  is with respect to the dominant gravity wave period.  $\mathbf{B}$  is the time average/ensemble average of the breaking velocity.

The boundary conditions at  $z = 0$  are

$$w^c(\mathbf{x}_h, 0, T) = \nabla \cdot \mathbf{M} - w^b(\mathbf{x}_h, 0, T), \quad \mathbf{M} = \overline{\mathbf{u}^w \eta^w}, \quad (19)$$

$$p(\mathbf{x}_h, 0, t) = \eta^c + p^a - P, \quad P = \left[ \frac{\partial \eta^w}{\partial \tau} \right]^2, \quad \text{and} \quad (20)$$

$$\begin{aligned} \nu \left( \frac{\partial \mathbf{v}^c}{\partial z} + \mathbf{S} \right) \Big|_{z=0} = & \left( \tau - \nu \frac{\partial \mathbf{b}}{\partial z} \Big|_{z=0}, \right. \\ \mathbf{S}(\mathbf{x}_h, t) = & \left. \frac{\partial^2 \mathbf{u}^w(\mathbf{x}_h, 0, t)}{\partial z^2} \eta^w(\mathbf{x}_h, t), \right. \end{aligned} \quad (21)$$

the sea elevation  $\eta$  being expressed in terms of the sum of the wave-associated component, with superscript  $w$

and the current-associated component identified with superscript  $c$ .

Next, we derive the slow-time tracer equation and thereby an equation for the evolution of the buoyancy. The tracer Eq. (3) is

$$\frac{\partial \theta}{\partial t} + \epsilon^2 \frac{\partial \theta}{\partial T} = -\epsilon(\mathbf{u}^w + \epsilon^2 \mathbf{v}^c + \epsilon^2 \mathbf{b}) \cdot \nabla \theta + \epsilon^2 Q, \quad (22)$$

as a consequence of (10) and (6). Expanding  $\theta = \theta_0 + \epsilon \theta_1 + \dots$  and substituting into (22), the balance of terms leads to  $\theta_0 = \theta_0(\mathbf{x}_h, z, T)$ , to lowest order. Integration in time of the next-order balance yields

$$\theta_1 = -\mathbf{U} \cdot \nabla \theta_0, \quad (23)$$

which implies that  $\langle \theta \rangle = \theta_0 + O(\epsilon)$  and  $\theta' = \epsilon \theta_1 + O(\epsilon^2)$ .

The  $t$  average of (22), followed by the ensemble average yields

$$\frac{\partial \theta_0}{\partial T} + (\mathbf{V}^c + \mathbf{B}) \cdot \nabla \theta_0 = \langle Q \rangle. \quad (24)$$

The tracer surface boundary condition (5) is

$$k \frac{\partial \theta_0}{\partial z} = T \quad \text{at} \quad z = 0, \quad (25)$$

to lowest order.

### b. The breaking-generated diffusion

We now address the parametric construction of the stress term  $\mathbf{R}^c$  in (1) and (18). We adapt the approach of Sullivan et al. (2007) under some modifications to apply it to the dynamics of waves, currents, and breaking. Let

$$\nabla \cdot \mathbf{R}^c := \frac{2}{3} \nabla e,$$

where  $e$  is the fluctuation kinetic energy. The turbulent kinetic energy (TKE) equation for  $e$ , given in Ferziger and Peric (1997, pp. 273–275), modified to include the effect of the Stokes drift  $\mathbf{u}^{\text{St}}$  and the breaking velocity mean  $\mathbf{B}$ , becomes

$$\frac{\partial e}{\partial t} = \dots - (u_j^{\text{St}} + B_j) \frac{\partial e}{\partial x_j} - \tau_{i,j} \frac{\partial (u_j^{\text{St}} + B_i)}{\partial x_j} + W,$$

where for  $i, j = 1, 2, 3$ ,

$$\tau_{i,j} = \frac{1}{2} \mu_b \left[ \frac{\partial (B_i + V_i^c)}{\partial x_j} + \frac{\partial (B_j + V_j^c)}{\partial x_i} \right].$$

Here,  $\mu_b = C_b \ell_b e^{1/2}$ , where  $C_b$  is an empirical parameter, and we use the Reynolds decomposition,  $\mathbf{b} := \mathbf{B} + \mathbf{b}'$ .

The mixing length is proportional to the amplitude of the waves,

$$\ell_b = \gamma \sqrt{\int_0^\infty f(\sigma) d\sigma}, \quad (26)$$

where  $\gamma$  is an empirical parameter, and  $f(\sigma)$  is the wave spectrum. (Unless the boundary layer dynamics were resolved in the model, the choice of length scale will not make a great deal of difference, after tuning is done. However, we acknowledge that our choice is not the conventional one.) The source term  $W$  in (26) is found by taking the difference between the transport of  $\mathbf{A}$  and its mean field  $W = \langle \mathbf{b}' \cdot \mathbf{A} \rangle$  (see Sullivan et al. 2007), where  $\mathbf{A} := \mathbf{b} \times \mathbf{Z}^c + \mathbf{b} \times (\mathbf{V} \times \mathbf{b}) + \mathbf{V}^c \times (\mathbf{V} \times \mathbf{b}) - 1/2 \mathbf{V} |\mathbf{b}|^2$ .

The  $j$ th component of the tracer wave diffusion term  $\mathbf{Q}$  in (24) is given by

$$Q_j = \frac{\partial}{\partial x_j} \left[ -\overline{\langle \theta' b_j' \rangle} + \mu_\theta \frac{\partial \theta_0}{\partial x_j} \right],$$

where  $\mu_b = C_\theta \ell_b e^{1/2}$ , with  $C_\theta$  as another empirical constant.

### 3. Parameterization of wave breaking

With the specification of the field  $\mathbf{b}$ , we obtain a complete description of the large-scale equations of motion and boundary conditions. There are two aspects of the random process  $\mathbf{b}$  that are essential to the construction of the breaking-generated momentum conversion and wave-breaking diffusion terms: the space–time locations where  $\mathbf{b}$  is nonzero and the distribution of its local magnitude and direction. One way to pin down  $\mathbf{b}$  is to construct a statistical multiparametric model of the filtered total velocity  $\mathbf{q}$  field data. Whether statistical stability is practically possible in computing mean breaking fields from data largely depends on the extent of the domain of interest and the whitecapping dynamics.

Our approach is to produce a parameterization that blends wave-breaking kinematics and statistical models. There are four components to our approach: 1) we adopt an empirical model for individual breaking events; 2) we propose a model that predicts the occurrence of breaking events, based upon the dynamics of wave groups and its empirical relation to the occurrence of breaking; 3) we develop a probabilistic setting that predicts the spatiotemporal distribution and strength of breaking events, based upon energetics; and 4) we upscale the collective microdynamics, yielding a macroscopic-scale breaking velocity field  $\mathbf{b}$  with dynamics at the spatiotemporal scales of the currents.

#### Empirical model for individual breaking events

Sullivan et al. (2004) suggested a parametrization of breaking events, inspired by experiments conducted in the laboratory. We use a simplified version of this parametrization in what follows.

We take the direction of wind propagation as  $\mathbf{a} = (\cos\phi, \sin\phi, 0)$ . Let us further suppose that the wave breaks are at position  $\mathbf{X} = (X, Y)$  and at time  $t_b$ . The force associated with this single breaking event is assumed to be directed in the horizontal direction  $\mathbf{a}$ , and following Sullivan et al. (2004), can be described mathematically by

$$\mathcal{A} = k_b \frac{g}{2\pi} \mathcal{X}(\beta) \mathcal{Y}(\delta) \mathcal{Z}(\gamma) \mathcal{T}(\alpha) \mathbf{a}, \quad (27)$$

where

$$(\alpha, \beta, \delta, \gamma) = \left( \frac{t - t_b}{T_w}, \frac{x - X}{ct}, \frac{2(y - Y)}{\lambda}, \frac{z}{\chi ct} \right) \quad (28)$$

are the dimensionless time and space coordinates, local to the breaking event, and

$$\begin{aligned} \mathcal{X} &= 5.34\beta^3(1 - \beta^2), & 0 \leq \beta \leq 1, \\ \mathcal{Y} &= 1 - (\delta - 1)^4, & 0 \leq \delta \leq 2, \\ \mathcal{Z} &= (1 - \gamma^4)^2, & -1 \leq \gamma \leq 0, \\ \mathcal{T} &= 25\alpha(1 - \alpha)e^{-3.4\alpha}, & 0 \leq \alpha \leq 1. \end{aligned} \quad (29)$$

The multiplier  $k_b$  is the strength of breaking, and the constant  $0 < \chi < 1$  is the aspect ratio of the depth to the length of the breaker. [The parameterization for the functions in (29) is simpler than originally proposed in Sullivan et al. (2004), but nevertheless, it is qualitatively similar.]

The *breaker velocity* field  $\tilde{\mathbf{b}}(\alpha, \beta, \delta, \gamma)$  associated with a particular breaking event is obtained by solving the Navier Stokes equations with a body force given by (27), with suitable boundary conditions. Here, we simplify this calculation and propose that the breaker velocity be given by the initial boundary value problem

$$\partial_\alpha \tilde{\mathbf{b}} = \frac{1}{Re} \Delta_{\beta, \delta, \gamma} \tilde{\mathbf{b}} + \mathcal{A}, \quad \nabla_{\beta, \delta, \gamma} \cdot \tilde{\mathbf{b}} = 0. \quad (30)$$

Here,  $\Delta_{\beta, \delta, \gamma}$  is the Laplacian operator and  $\nabla_{\beta, \delta, \gamma}$  the divergence operator, respectively, in the scaled variables. The boundary conditions on  $\tilde{\mathbf{b}}$  are periodic in  $\delta$ , and  $|\tilde{\mathbf{b}}| \rightarrow 0$  as  $\beta, \gamma \rightarrow \pm\infty$ .

For illustration let us assume that  $\tilde{\mathbf{b}} = (b_1, 0, b_3)$  (thus the incidence angle is  $\phi = 0$ ) and choose  $k_b = 0.18$  and  $\chi = 0.2$  with  $Re = 3000$  (based on wave scales and the kinematic viscosity). The Fourier-series solution to (30)

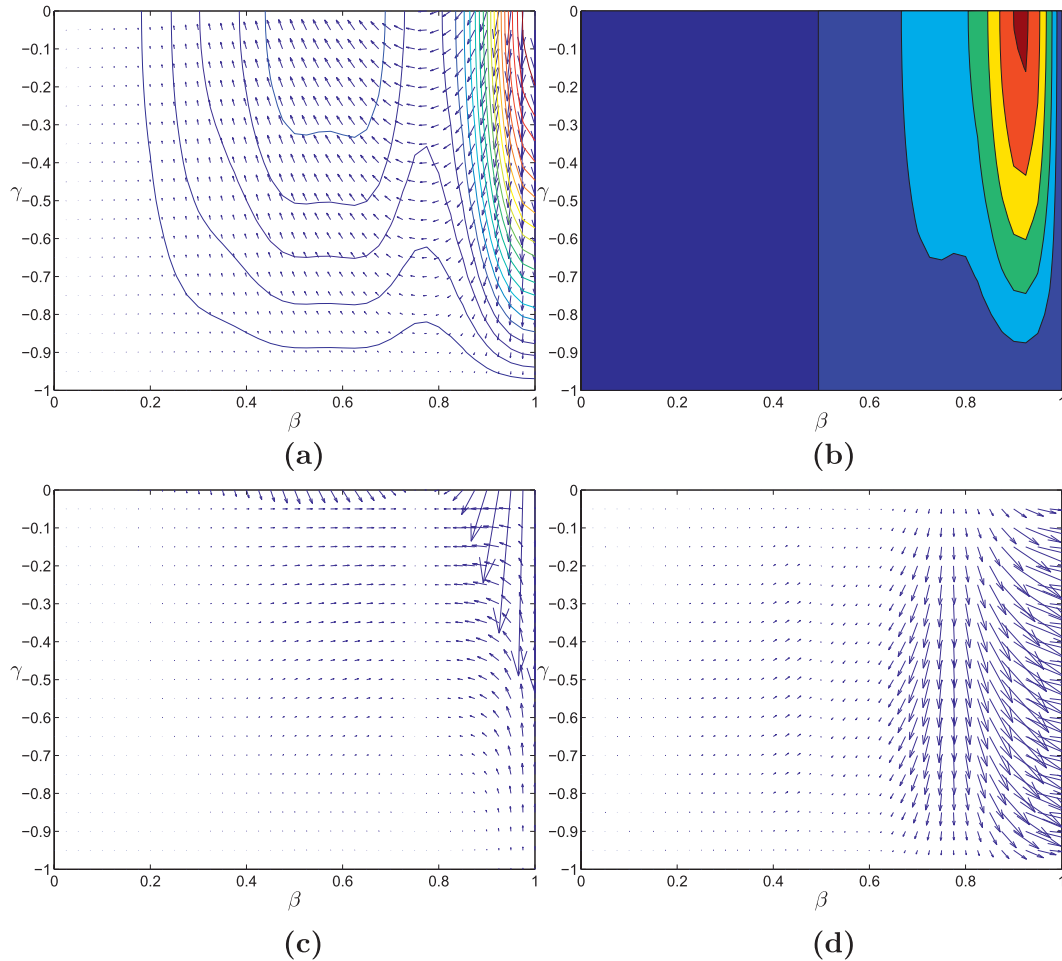


FIG. 1. Nondimensional plots of fully developed breaker velocity and associated fields in the  $(\beta, \gamma)$  plane: (a) the breaking velocity  $\mathbf{b}$ , (b) vorticity  $\mathbf{V} \times \mathbf{b}$ , (c)  $\mathbf{V}|\mathbf{b}|^2$ , and (d)  $\mathbf{b} \times \mathbf{V} \times \mathbf{b}$ .

yields the fields pictured in Fig. 1. The time dependence of each breaking event is of little concern at current time scales and thus omitted in this presentation. (According to Sullivan et al. (2004), a breaking event grows and decays exponentially in time.)

### 1) WAVE GROUPS AND WAVE BREAKING

In Song and Banner (2002) and Banner and Peirson (2007), the authors propose that the onset of wave breaking in deep-water wave groups of weakly nonlinear unidirectional Stokes waves can be determined from the mean convergence rate of wave energy and geometrical steepening following the wave group maxima. Here, we develop a strategy to evaluate the occurrence of breaking events from realizations of a random sea surface, where the breaking can result more rapidly from local wave energy convergence owing to nonlinearity during the superposition of free wave modes. Song and Banner (2002) also included a variant of this

mechanism (a chirped wave packet) in their study. It is not known which of these routes to breaking is more prevalent in the ocean. In any event, using the formulation of the evolving wave field described below can result in a faster time scale for fluctuations in  $\mu(t)$  because of the broader spectral bandwidth and directionality of the free wave modes. Further, the lack of uniformity in the wave field clearly evident in Fig. 2 can cause fluctuations in  $\mu(t)$  at the evolving wave group maximum. We note finally that the effect of longer waves on the breaking propensity of the smaller waves (e.g., Phillips and Banner 1974) is not included.

We assume the water surface of the ocean is described by a zero-mean Gaussian random process denoted by  $(\mathbf{x}, t)$ : the surface elevation is

$$\eta(\mathbf{x}, t) = \text{Re} \left\{ \int_{\mathbb{R}^2} e^{i(\mathbf{k} \cdot \mathbf{x} + \sigma t)} \sqrt{\Gamma_\eta(\mathbf{k})} \mathbb{W}(\mathbf{d}\mathbf{k}) \right\} := \text{Re} \{ \eta^*(\mathbf{x}, t) \}, \tag{31}$$

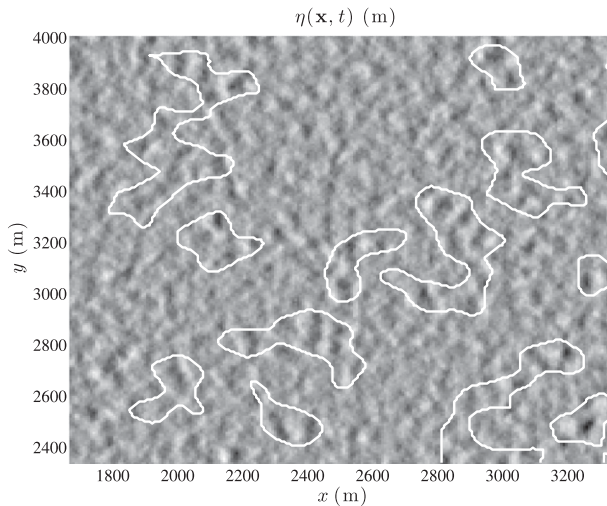


FIG. 2. Simulated ocean surface and boundary of detected wave groups in a subregion of the modeling area for a fixed time step.

where  $\mathbb{W}$  is a complex-valued white-noise measure on  $\mathbb{R}^2$ , such that

$$\langle \mathbb{W}(d\mathbf{k}), \overline{\mathbb{W}(d\mathbf{k}')} \rangle = \delta(\mathbf{k} - \mathbf{k}') d\mathbf{k} d\sigma; \quad (32)$$

and the spectral distribution  $\Gamma_\eta(\mathbf{k}, \sigma)$  is the Fourier transform of the covariance function

$$\begin{aligned} \Gamma_\eta(\mathbf{x}', t') &= \langle \eta(\mathbf{x}, t)\eta(\mathbf{x} + \mathbf{x}', t + t') \rangle \\ &= \text{Re} \left[ \int_{\mathbb{R}^2} e^{i(\mathbf{k}\cdot\mathbf{x}' + \sigma t')} \Gamma_\eta(\mathbf{k}) d\mathbf{k} \right]. \end{aligned} \quad (33)$$

We assume that the waves, to leading order, are linear and uninfluenced by the ocean bottom, and hence the wave frequency satisfies the deep-water dispersion relation

$$\sigma = \sigma(\mathbf{k}) = \sqrt{gk}. \quad (34)$$

The waves are assumed to have local horizontal wavenumber  $k$ , and speed  $c = \sqrt{g/k}$ . The associated wavenumber magnitude, wave period, and wavelength, respectively, are  $k = |\mathbf{k}|$ ,  $T_w = (2\pi)/\sqrt{kg}$ , and  $\lambda = (2\pi)/k$ .

Wave groups are numerically characterized through an envelope surface of  $\eta$  in an analogous fashion to the one-dimensional situation considered by Longuet-Higgins (1984). For each value of  $t$ , the envelope surface  $\rho(\cdot, t)$  is obtained by applying a low-pass spatial filter to  $|\eta^*(\cdot, t)|$ . A wave group is then defined as a connected component of the excursion set  $\{\mathbf{x} : |\rho(\mathbf{x}, t)| > \rho^*\}$ , where  $\eta$  attains at least one positive maximum.

The threshold  $\rho^*$  may be determined as follows: regard  $\rho(\mathbf{x}, t)$  as the norm of a complex Gaussian (sea elevation) field, and take the average Euler characteristic, denoted  $\chi_{\text{Eu}}(\rho^*)$ , of the excursion sets  $\{\mathbf{x} : \rho(\mathbf{x}, t) > \rho^*\}$ .

The Euler characteristic is a topological property with the following feature: if a set has  $n$  connected components with a total of  $m$  holes in them, its Euler characteristic is equal to  $n - m$ . The definition of  $\chi_{\text{Eu}}$  for general sets and manifolds and further properties can be found in Adler and Taylor (2007). Moreover, analytic expressions for the expected value of the characteristic number of excursion sets of general Gaussian processes and their complex norm are known (see Adler 1978). In particular, the mean  $\langle \chi_{\text{Eu}}(\rho^*) \rangle$  is zero for  $\rho^* = \sqrt{\langle \rho^2 \rangle}$ , and attains its only positive maximum at  $\rho^* = \sqrt{\langle \rho^2 \rangle (1 + 2\langle \rho^2 \rangle)}$ . We propose taking  $\rho^*$  between these two extrema,

$$\rho^* = (1 - \alpha)\sqrt{\langle \rho^2 \rangle} + \alpha_\rho \sqrt{\langle \rho^2 \rangle (1 + 2\langle \rho^2 \rangle)}, \quad (35)$$

for an empirical value of  $\alpha_\rho \in [0, 1]$ .

The local wave energy is parameterized in Song and Banner (2002) by

$$\mu(t) := \eta^2(\mathbf{x}_{\text{max}}, t) \mathbf{k}^2(\mathbf{x}_{\text{max}}, t), \quad (36)$$

where  $k$  is the local wavenumber, and  $\mathbf{x}_{\text{max}} = \mathbf{x}_{\text{max}}(t)$  is the position of the maximum crest in the group. The non-dimensional parametric mean growth rate of wave group energy is defined as

$$\delta(t) = \frac{1}{\langle \sigma \rangle} \frac{D\mu}{Dt}, \quad (37)$$

where the material derivative is taken following the wave group, and  $\langle \sigma \rangle$  is the average frequency. Song and Banner (2002) identify a threshold  $\delta^* \approx 1.4 \times 10^{-3}$  for  $\delta$  that distinguishes breaking from nonbreaking wave groups.

For each fixed wave group, the start of a breaking event is defined as time  $t = t_b$  of the first upcrossing of the threshold  $\delta^*$  by  $\delta(t)$ . We assume the duration of the event is, on average, one wave period  $T_w$ . The position of the breaking event is  $\mathbf{X} = \mathbf{x}_{\text{max}}(t_b)$ .

The strength of breaking  $k_b$ , see (27), is determined by equating the total kinematic energy from the velocity field in (30) with the total drop of energy during breaking. Let  $E(t), t > t_b$ , be the energy of  $\mathbf{b}$  per unit of area transverse to the propagation direction; namely,

$$E(t) = \rho_0 c \frac{1}{\lambda ct} \int_0^t \int_{\Omega^b} \int_{-\chi^{ct}}^0 \mathcal{A}(\mathbf{x}, z, s) dz d\mathbf{x} ds, \quad (38)$$

where  $\Omega^b$  is the (time-dependent) horizontal support of  $\mathbf{b}$ ,

$$\Omega^b(t) = [0, ct] \times [-\lambda/2, \lambda/2]. \quad (39)$$

Using (29), the total energy gives

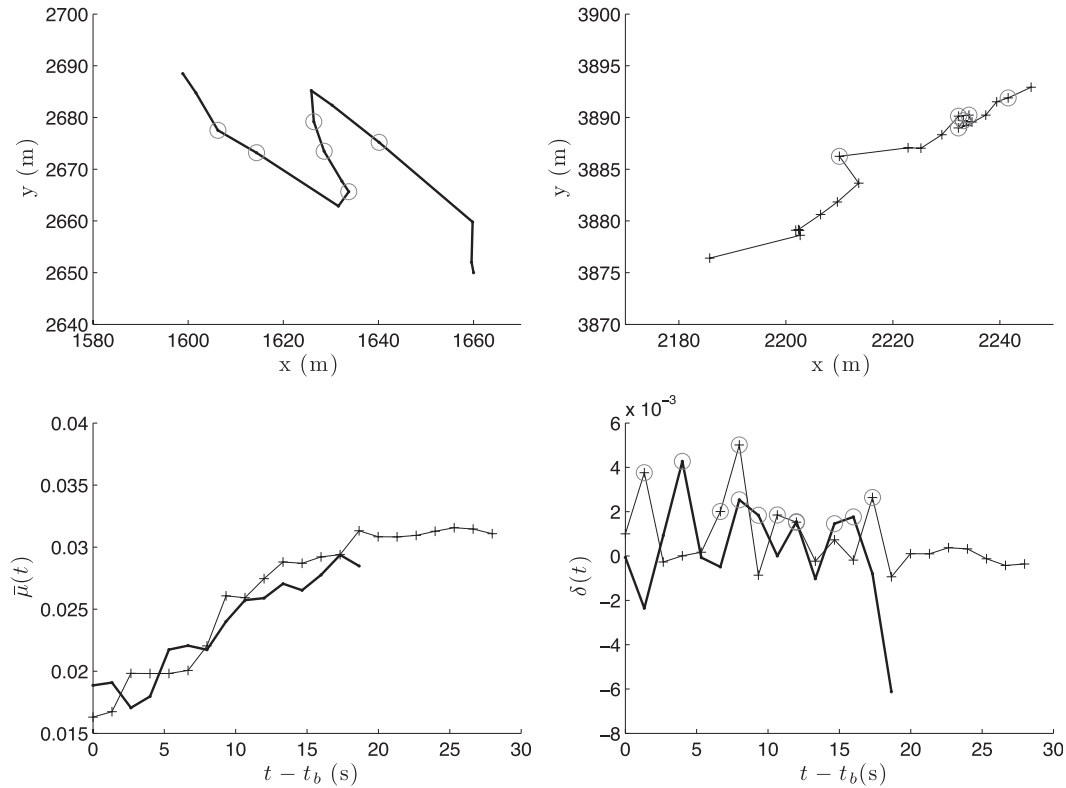


FIG. 3. Examples of two typical simulated breaking wave groups. (top) The trajectory of the centroid of the wave groups is shown: (top left) the wave group is moving in the southeast direction and (top right) the trajectory moves toward the northwest. Red circles correspond to time points where  $\delta(t) > \delta^* = 1.4 \times 10^{-3}$ . (bottom left) The growth of the smoothed running average of the local wave energy parameter is shown. A bold line is used for the first tracked wave group and crosses to indicate the second. (bottom right) The energy convergence rate  $\delta(t)$  is plotted. It should be noted that each of the groups is considered to have had one single breaking event during the timeframe plotted. Quantities associated with these breaking events, for example,  $k^*$  or  $k_b$ , are computed as the time average over the points where  $\delta(t) > \delta^*$ .

$$E(T_w) = \frac{0.55g\rho_0\chi k_b}{k^2}. \tag{40}$$

On the other hand, as reported in Banner and Peirson (2007) and Tian et al. (2008), the mean drop in total wave energy can be computed from the convergence rate  $\delta$  and the wave energy just prior to breaking, as

$$E(T_w) = c_E g \rho_0 \eta^2(\mathbf{x}_{\max}, t_b) [\delta(t_b) - \delta^*], \tag{41}$$

where  $c_E$  is an empirical parameter taken here to be  $c_E = 55$  as in Tian et al. (2008). One then can use (40) to solve for  $k_b$ , and this yields

$$k_b = \frac{1.8c_E}{\chi} k^2 \eta^2(\mathbf{x}_{\max}, t_b) [\delta(t_b) - \delta^*]. \tag{42}$$

## 2) PARAMETRIC LOCALIZATION OF WAVE BREAKING

The location in space–time of breaking events on the ocean surface is modeled by a Poisson-point process

$L = \{(\mathbf{X}, t_b)\}$  of locations  $\mathbf{X} \in \mathbb{R}^2$  and times  $t_b > 0$ . The process  $L$  is characterized by its constant intensity  $\Lambda > 0$ , defined as follows. Let  $A \subset \mathbb{R}^2$  be some region of the ocean surface and  $[T_1, T_2]$  a time interval. If  $N(A \times [T_1, T_2])$  denotes the number of breaking events that occur in region  $A$  and between times  $T_1$  and  $T_2$ , then

$$\Lambda = \frac{\langle N(A \times [T_1, T_2]) \rangle}{(T_2 - T_1)\text{area}(A)}. \tag{43}$$

To a breaking event, say at  $(\mathbf{X}, t_b) \in L$ , we associate a velocity perturbation given at  $t$  time scales by  $\tilde{\mathbf{b}}_{\mathbf{p}}(\mathbf{x} - \mathbf{X}, z, t - t_b)$  defined via (30). The subindex  $\mathbf{p}$  simply denotes that the vector field  $\tilde{\mathbf{b}}_{\mathbf{p}}$  is characterized by random “breaking parameters”  $\mathbf{p} = (k(t_b), k_b)$  independent of the position of the breaker and of known probability density. Furthermore,  $\tilde{\mathbf{b}}_{\mathbf{p}}(\mathbf{x}, z, t)$  is nonzero only for  $\mathbf{x} - \mathbf{X} \in \Omega^b(T_w)$ ,  $z \in [-\chi c T_w, 0]$ , and  $t - t_b \in [0, T_w]$ , where  $\Omega^b(t) = \Omega^b(\mathbf{p}, t)$  is given by (39).

The perturbation at  $T$  time scales associated to a wave breaking event is

$$\bar{\mathbf{b}}_{\mathbf{p}}(\mathbf{x}, z) := \frac{1}{T_w} \int_0^{T_w} \tilde{\mathbf{b}}_{\mathbf{p}}(\mathbf{x}, z, t) dt, \quad (44)$$

and the total breaking velocity field is the random sum

$$\mathbf{b}(\mathbf{x}, z, T) = \sum_{(\mathbf{x}, t_b) \in L} \bar{\mathbf{b}}_{\mathbf{p}}(\mathbf{x} - \mathbf{X}, z) \delta(T - t_b). \quad (45)$$

#### 4. Examples of waves, currents, and breaking

##### a. Wave-breaking simulation

The complex surface field  $\eta^*(\mathbf{x}, t)$  is obtained by performing a two-dimensional (fast) inverse Fourier transform as indicated in (31). For the energy spectrum in (33), we chose  $\Gamma_{\eta}(\mathbf{k}) = 2\Psi(\mathbf{k})$ , where  $\Psi$  is the omnidirectional and wind-dependent spectrum proposed in Elfouhaily et al. (1997) with inverse wave age  $\Omega_w = 1.3$  and wind speed  $U_{10} = 15 \text{ m s}^{-1}$ . The resulting peak wavenumber is  $k_p := [g/(U_{10}\Omega_w)]^2 = 0.074 \text{ m}^{-1}$ . We consider a symmetric wavenumber grid with  $512 \times 512$  values, spaced by  $dk_x = dk_y = 0.0063 \text{ m}^{-1}$  and spanning between zero and a maximum of  $0.4 \text{ m}^{-1}$ . The resulting spatial discretization has  $dx = dy = 7.8 \text{ m}$  and a total extension of  $4000 \text{ m}$ . Temporal frequencies are computed as  $\sigma = (gk)^{1/2}$ , which yields  $\langle\sigma\rangle = 0.98 \text{ s}^{-1}$  and a simulation time step of  $\Delta t = 0.67 \text{ s}$ . The wave-breaking simulation was run for  $5000 \text{ s}$ .

The computation of the wavenumber  $k(t) = \sqrt{k_x^2 + k_y^2}$  at the local maxima of  $\eta(\cdot, t)$  is performed by making  $k_x = (2\pi)/l_x$ , where  $l_x$  is the distance between the consecutive upcrossing and downcrossing of the level  $z = 0$  to the right and left of the local maximum in the  $x$  direction. The same procedure is applied in the  $y$  direction to obtain  $k_y$ .

A Hamming window for wavenumbers satisfying  $k < 0.4k_p$  was used to filter  $|\eta^*(\cdot, t)|$  to obtain the envelope surface  $\rho(\cdot, t)$ . The threshold value for wave group detection  $p^*$  is obtained by making  $\alpha_p = 0.5$  in (35). Wave groups are defined as connected components of the excursion set  $\{\mathbf{x} : |\rho(\mathbf{x}, t)| > p^*\}$  with the following properties: at least one positive maximum of  $\eta$  belongs to the excursion set, and the extent of the set in each direction is at least  $\epsilon_g [(2\pi)/k_p]$ , where  $\epsilon_g$  is a size parameter taken as  $\epsilon_g = 1.5$  in this example. The filtering window, the value of  $\alpha_p$ , and the size parameter  $\epsilon_g$  are chosen so the simulated wave groups exhibit shapes and sizes similar to those of oceanic wave groups observed in nature (as reported in Niedermeier et al. 2005). Figure 2 shows the generated field  $\eta(\cdot, t)$  for a fixed  $t$  and the boundaries of the detected wave groups.

The location of a wave group is tracked in time by the position of its centroid  $\mathbf{x}_{\text{cen}}(t)$ . Wave groups at  $t$  and  $t + \Delta t$  are considered subsequent stages of the same wave group if  $|\mathbf{x}_{\text{cen}}(t) - \mathbf{x}_{\text{cen}}(t + \Delta t)|$  is of the order  $\bar{c}\Delta t$ ,

where  $\bar{c}$  is the mean speed of the group. Groups whose lifetimes are less than  $t_g$  times its mean period  $\langle T \rangle = \langle 2\pi[kg]^{-1/2} \rangle$  are discarded.

As discussed in Song and Banner (2002), the calculation of  $\langle\mu(t)\rangle$  and its material derivative are challenging because of the oscillatory nature of  $\mu$ . To circumvent that problem, the evaluation of the condition  $\delta(t) > \delta^*$  on individual wave groups is performed as follows: 1) the moving average  $\bar{\mu}(t)$  of  $\mu$  is computed, and this moving average does not contain the oscillations found in  $\mu$ ; 2) a smoother version of  $\bar{\mu}$ , denoted as  $\bar{\mu}^*(t)$ , is computed by fitting a cubic spline at time points sampled every one tenth of  $\langle T \rangle$ ; 3)  $\delta(t)$  is computed as the polynomial derivative of  $\bar{\mu}^*$ ; and 4) breaking events are those for which  $\delta(t) > \delta^*$ . To remove endpoint effects of the weighted average and the polynomial fitting, breaking events that include the endpoints of the time series are suppressed. The final result of the simulation are as follows: the intensity measure  $\Lambda$  and the sample joint distribution of the pair  $\mathbf{p} = (k^*, k_b)$ , where  $k^* = k(t_b)$  is the wavenumber at breaking maxima, and  $k_b$  is the breaking strength parameter defined in (42). These statistics are used to generate random momentum contributions given by (27) at random positions in space–time.

The local wavenumber at a breaking event  $k^*$  is computed by taking the mean of  $k(t)$  at the maximum of the wave group over the times where  $\delta(t) > \delta^*$ . We obtain a mean value of  $\langle k^* \rangle = 0.082 \text{ m}^{-1}$ . The breaking strength parameter  $k_b$  is then computed using (42), with a value for the breaker aspect ratio of  $\chi = 0.2$  as in Sullivan et al. (2004). We obtain a mean value  $\langle k_b \rangle = 0.055$ , which falls into the range of values  $0 < k_b < 0.36$  proposed by Sullivan et al. (2004). Figure 3 shows the space–time evolution and the time evolution of two centroids of typical simulated breaking events. The local wave energy and the mean growth rate are also shown.

Figure 4 shows the marginal histograms for the magnitude of the mean wavenumber during a breaking event and the breaking strength parameter.

The total number of groups that exhibited breaking events was 6021 out of 16590 groups tracked. The resulting intensity measure is  $\Lambda = 3.76 \times 10^{-8} \text{ m}^{-2} \text{ s}^{-1}$ .

The hypothesis of a Poisson distribution for  $L = \{(\mathbf{X}, t_b)\}$  (the spatiotemporal position of breaking events) can be easily tested. Following Illian et al. (2008), one can define

$$l(r) = \left[ \frac{3\langle N(B_r) \rangle - 1}{4\pi\Lambda} \right]^{1/3}, \quad (46)$$

where  $N(B_r)$  denotes the number of points in  $L$  such that  $|(\mathbf{X}, t_b) - (\mathbf{x}_0, t_0)| < r$ , for any fixed reference  $(\mathbf{x}_0, t_0)$ . For a Poisson process  $l(r) = r$ . Figure 5 shows the comparison between the observed and theoretical  $l(r)$ .

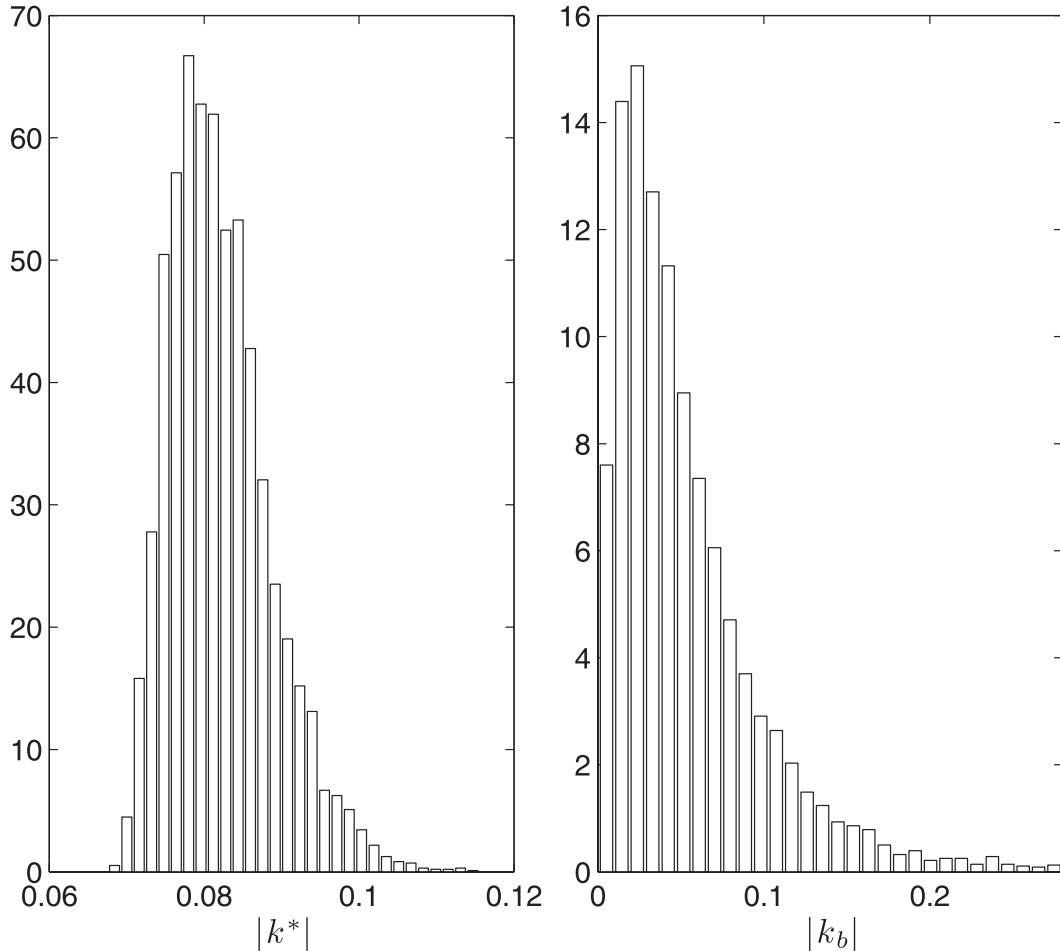


FIG. 4. Sample probability histograms for the mean wavenumber during breaking events and the breaking strength parameter.

Using (42), the contribution due to wave breaking to the total momentum flux via wind stresses at the ocean surface is

$$\begin{aligned} \langle \tau_b \rangle &= \rho_0 \Lambda \left\langle \int_0^{T_w} \int_{\Omega^b(\mathbf{p}, T_w)} \mathcal{A}(\mathbf{x}, s) \, d\mathbf{x} \, ds \right\rangle \\ &= 9.91 \sqrt{g} \rho_0 \Lambda \chi \langle k_b k^{-\tau/2} \rangle. \end{aligned} \tag{47}$$

The total momentum flux can be computed as  $\langle \tau \rangle = \rho_a C_d U_{10}^2$ , where  $C_d$  is the wave age-dependent drag coefficient (see Donelan 1982). For this particular example we used  $C_d = 1.84 \times 10^{-3}$ ,  $\chi = 0.2$ , and obtained  $\langle \tau \rangle = 0.497 \text{ kg m}^{-2} \text{ s}^{-1}$ ,  $\langle \tau_b \rangle = 0.209 \text{ kg m}^{-2} \text{ s}^{-1}$ .

Examples for seas at different states of aging and fixed  $U_{10} = 15 \text{ m s}^{-1}$  were also performed. The parameter values and results are summarized in Table 1.

*b. Breaking effects on currents*

In the following calculations, we will compare the relative roles of the Stokes drift velocity and the breaking

velocity on a cyclonic-current flow. Under natural circumstances both effects would be present. We solve (18) on a basin with periodic boundary conditions. The square domain was 56 km on each side. The domain was discretized in the  $X$  (horizontal in the figures) and  $Y$  directions generating a  $32 \times 32$  grid. The evolution equation for the currents was discretized, and a constant time step of 200 s was used in the upwinded/finite volume scheme for the vorticity. The velocity is computed from the potential and streamfunction from their respective elliptic equations. The total time of the calculation was approximately 12.8 h. This is a very short time span to see significant changes in the currents; however, the fact that the cyclone evolves little allows us to discern how the various velocity fields affect the outcomes.

Shown in Fig. 6a is the initial cyclonic vortex, which has a peak amplitude of  $5 \times 10^{-4} \text{ s}^{-1}$ . It has the shape of a two-dimensional Gaussian surface with characteristic width of 7 km. The associated velocity field is shown in Fig. 6b. In these calculations the gravity wave field was

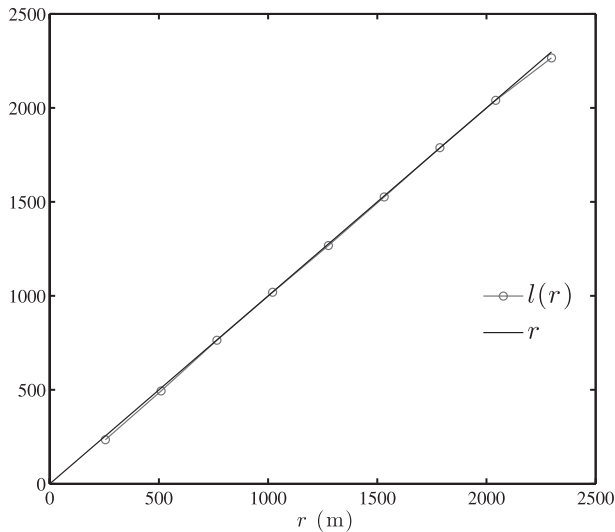


FIG. 5. Comparison between a statistic for  $l(r)$  and the identity function. See Illian et al. (2008) for details.

composed of deep-water waves that locally form wave groups and experience breaking events. The wave breaking field  $\mathbf{b}$  at the resolution of the current scales was found by the following upscaling procedure: 1) the number and location of breaking events ( $X, t_b$ ) are computed by generating realizations of a Poisson process with the calculated intensity measure,  $\Lambda$  in (43), over each element of the large-scale grid, and the duration of the large time step. 2) For each event, the values of the breaking parameters  $\mathbf{p} = (k(t_b), k_b)$  are drawn independently from its sample joint distribution (see Fig. 4). 3) For each generated event, the local velocity field  $\mathbf{b}$  in (45) and its curl are computed by solving (30). 4) At each point on the small grid, all the contributions by breaking events are averaged over the duration of the large time step. 5) The spatial mean is taken over the area encompassed by the element of the large-scale grid.

The velocity field associated with a breaking event has support given by (39). At the subgrid scale, these individual solutions are uncorrelated and smoothly connected. The magnitude and intensity of the averaged wave-breaking velocity has dimensionally appropriate intensities and magnitudes, without adjustable parameters.

In the calculations that follow, we omit the breaking-generated diffusion term; its effect is to diffuse away momentum, primarily at high frequencies, especially at breaking scales.

The Stokes drift corresponding to the random wave field was computed following Huang (1979). The resultant Stokes drift velocity, evaluated at the free surface is  $\mathbf{u}^{\text{St}}|_{z=0} := \mathbf{u}^{\text{St}} = (0.259, 0)$ ,  $w^{\text{St}} = 0$ . (directed from left to right in the plots).

TABLE 1. Simulation results for three different values of sea age and wind velocity  $U_{10} = 15 \text{ m s}^{-1}$ . The threshold energy convergence rate for wave breaking was kept constant at  $\delta^* = 1.4 \times 10^{-3}$ .

	1.0	1.3	1.6
$\Omega_w$	1.0	1.3	1.6
$K_p$ ( $\text{m}^{-1}$ )	0.043	0.073	0.11
$\alpha_p$	0.55	0.5	0.25
No. of groups	5569	16 590	36 916
No. of breaks	1646	6021	7255
$\Lambda$ ( $\text{m}^{-2} \text{ s}^{-1}$ )	$1.03 \times 10^{-8}$	$3.73 \times 10^{-8}$	$4.53 \times 10^{-8}$
$\langle k^* \rangle$ ( $\text{m}^{-1}$ )	0.066	0.082	0.113
$\langle k_b \rangle$	0.086	0.055	0.032
$C_d$	$1.30 \times 10^{-3}$	$1.84 \times 10^{-3}$	$2.19 \times 10^{-3}$
$\langle \tau \rangle$ ( $\text{kg m}^{-2} \text{ s}^{-1}$ )	0.35	0.49	0.59
$\langle \tau_b \rangle$ ( $\text{kg m}^{-2} \text{ s}^{-1}$ )	0.162	0.209	0.327

Figure 7 shows results for the evolution of the cyclone after 12.8 h of simulation, in the absence of the breaking velocity field. Figure 7a shows the vorticity field when the Stokes drift is present, and Fig. 7b shows the difference between the vorticity fields with and without vortex force. The picture shows the degree to which the Stokes drift affects the currents via the vortex force over a very short time span; its primary effect is to modify the resulting advection of the vorticity. Hence, on spatial spans on the order of tens of kilometers, and small time spans, the Stokes drift affects the advection of vorticity via the (conservative) vortex force in a very slight way, as expected.

Before considering the cyclonic-flow example, we illustrate what happens when the initial current velocity is zero everywhere. The plots in Fig. 8 show the velocity after 12.8 h of simulation. The vorticity and spectrum of vorticity are shown in Fig. 9. The combined effect of the Stokes drift velocity and breaking waves appears in the left column of Figs. 8 and 9. In contrast, the right-most plots in these figures show the corresponding results with the Stokes drift suppressed. The breaking of waves affects the velocity and vorticity fields considerably on a wide range of scales, as is evident from the spectral plots. Comparison of Figs. 8a and 9b show that these fields are more spatially homogeneous in the latter case, when the Stokes drift is zero. This is also shown in Figs. 9c and 9d, by way of the spectrum. The variance in both is comparable but there is a slight red shift in the mean of the spectrum along the  $X$  direction. More strikingly, there is a banded structure; the figures do not show that there are spectral components everywhere but there is an enhanced band in the  $X$  direction of wavenumber space, which is in the direction of the wind (the wind direction is imprinted in the currents via the breaking of the waves). The banded structure results from the  $X$  derivative of the vortex force. Since the breaking velocity is strictly directed in the  $X$  direction and it is

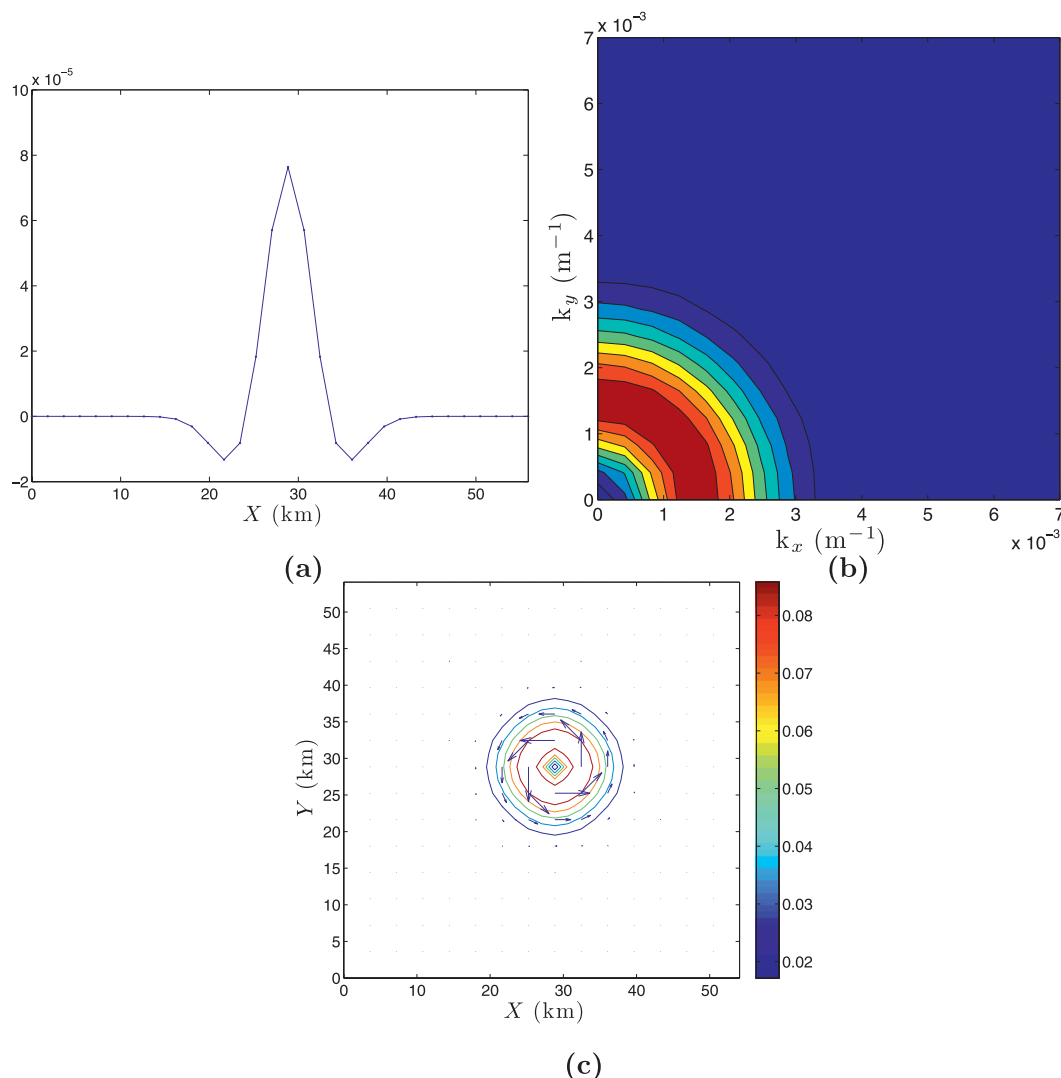


FIG. 6. (a) Cross section of symmetric Gaussian initial vorticity ( $\text{s}^{-1}$ ) at  $Y = 25$  km, (b) two-dimensional spectrum ( $\text{m s}^{-1}$ ) of the initial vorticity, and (c) the initial current velocity field  $\mathbf{v}^c$  ( $\text{m s}^{-1}$ ). The Stokes drift velocity primarily modifies the advection of vorticity.

only a function of the transverse coordinates, this  $X$  derivative is the only derivative in the curl of the vortex force that contributes to the vorticity equation.

Figures 10 and 11 show the effects of the breaking velocity and the Stokes drift on the dynamics of the cyclone, after 12.8 h of simulation. The initial conditions on the current are those appearing in Fig. 6. In Figs. 11a and 11d, we observe differences in the position of the cyclone center as well as differences in the spatial homogeneity in the structure of the flow itself. High vorticity is mostly concentrated close to the cyclone in the no-drift case (see Figs. 11b and 11e), and this is reflected in the respective spectra; there is a remnant of the spectrum of the vorticity of the cyclone shown in Fig. 6 for the nonbreaking case. The effect of the breaking

velocity on the currents via the breaking momentum flux terms is not gradual here; this results from the fact that the dominant time scales for breaking, waves, and currents are separated by two orders of magnitude. For every integration time step, which is 200 s long, there is an expected  $2.3 \times 10^4$  breaking event on the whole of the simulation domain, since the intensity measure  $\Lambda = 3.76 \times 10^{-8} \text{ m}^{-2} \text{ s}^{-1}$ .

It is clear that the advection of the vortical structure is the result of the Stokes drift velocity, however, the breaking velocity has a significant effect on the dynamics of the cyclone as well. Figures 11c and 11d have the banded spectra described before, and the direction of the wind is again evident in these plots. The variance is smaller in Fig. 11c, when the drift velocity is present.

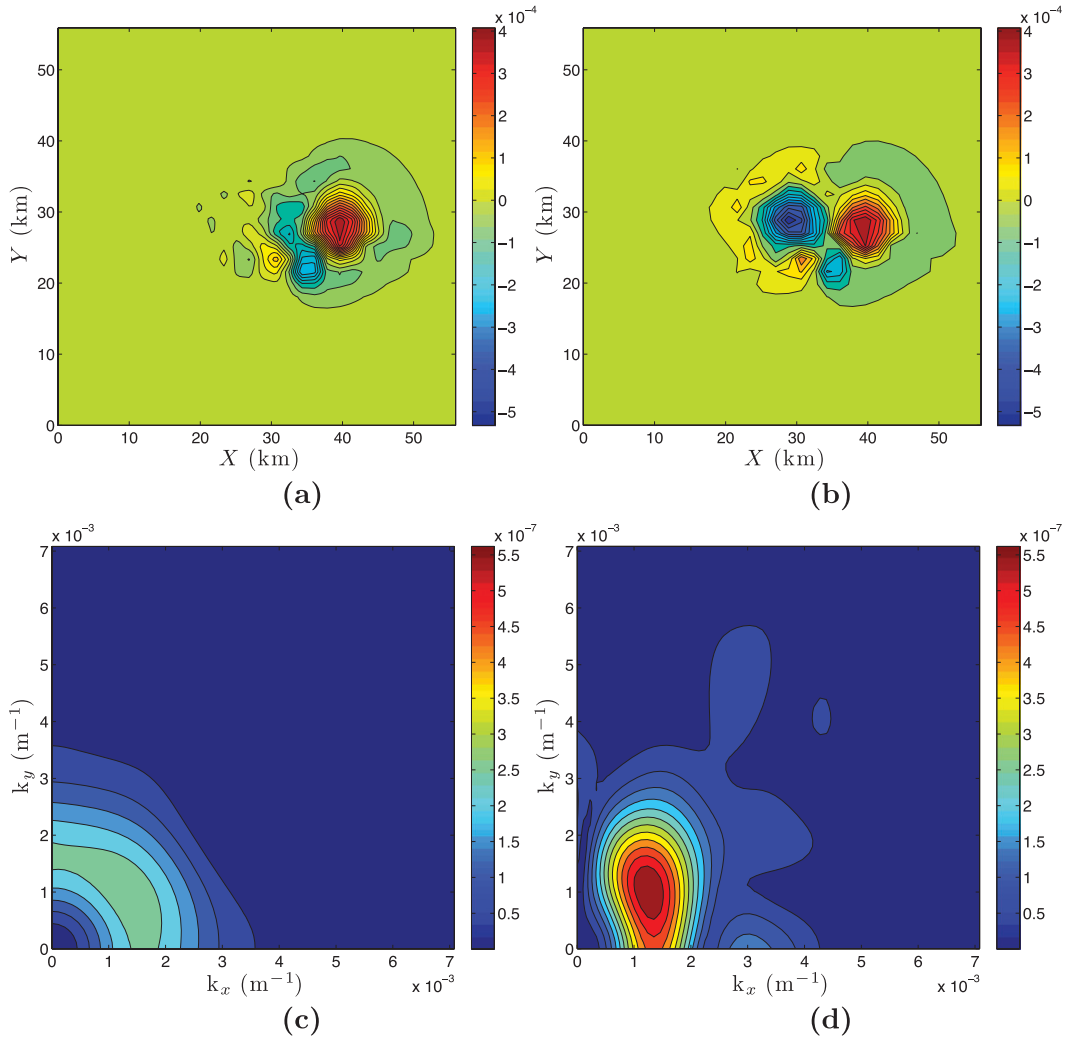


FIG. 7. Results after 12.8 h of simulation with the cyclonic initial condition as shown in Fig. 6. No breaking is present. (a) Vorticity  $Z^c(\mathbf{X})$  ( $\text{s}^{-1}$ ) and (c) spectrum ( $\text{m}^2 \text{s}^{-1}$ ) of vorticity with Stokes drift equal to  $\mathbf{u}^{\text{St}} = (0.259, 0) \text{ m s}^{-1}$ . (b) The difference vorticity field between the case with Stokes drift and without; (d) the spectrum of that difference. Note the difference in amplitude scale in (a) and (b). Also note in (d) the effect of the advection due to the Stokes drift.

Remnants of the spectrum of the cyclone are evident, especially in the lower low-wavenumber regime in Fig. 11d. We tracked the maximum speed of the flow, over a 12.8 h integration, to get a qualitative assessment of the overall advection of the same initial cyclone, under the same Stokes drift velocity. In the absence of breaking, the cyclone moved, approximately, a total of 10 and 0 km, respectively, when the drift velocity was present and otherwise. With breaking present, these numbers changed to 11.5 and  $-2$  km (to the left of its initial position), respectively. These are signed distances between initial and final positions, rather than the length of the cyclone track. In the absence of breaking, we found the expected enhancement on the advection of the cyclone

by the presence of the  $X$ -directed drift velocity. The presence of breaking stalled the cyclone, when breaking and the Stokes drift were present.

Figures 12a and 12c show the mean rate of displacement of 32 tracer particles in the flow, initially placed at 5 km from the origin of the cyclone and arranged symmetrically. The difference between Fig. 12a and Fig. 12c is that in the latter we increased the overall  $k_b$  strength at all wavenumbers by a factor of about 5. (The reason we gave the stronger breaking case consideration is because we wanted to infer the asymptotic behavior of the rate; the small spatial domain and periodic boundary conditions lead to the fields self interacting sometime after about 7 h.) The displacement

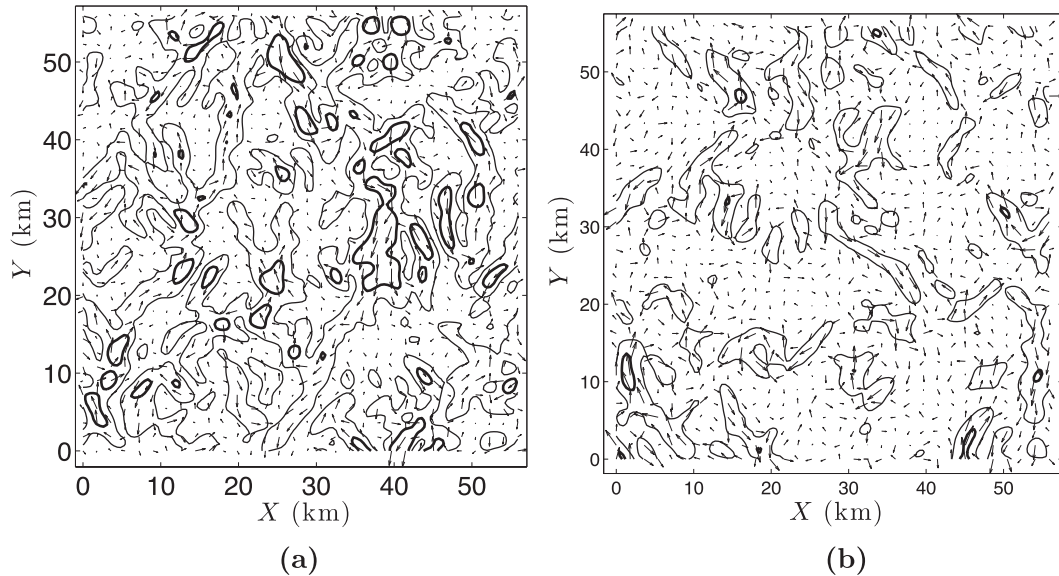


FIG. 8. Results after 12.8 h of simulation with an initially zero velocity field. Velocity contours ( $\text{m s}^{-1}$ ): (a) corresponding to the case  $\mathbf{u}^{\text{St}} = (0.259, 0) \text{ m s}^{-1}$ , (b) zero Stokes drift. A comparison of (a) and (b) shows that the former is less spatially homogeneous and this is due to the presence of the drift velocity. Magnitude of the velocity contours at 0.05 (lighter) and 0.1  $\text{m s}^{-1}$  drawn.

was computed as the Euclidean distance of the particle relative to its initial position. This distance is averaged over all particles, and then its time derivative is approximated and defined here as the rate. The different rate curves in Figs. 12a and 12c correspond to different flow conditions. Lighter curves correspond to a case with no drift velocity present, dark curves with Stokes drift. The lower thin curves were obtained from the zero initial conditions run highlighted in Fig. 7; the two curves show comparable transport rates. For the remaining curves we have the comparison of breaking and nonbreaking cases. Nonbreaking rates are depicted with circles, and the significantly noisier heavy solid lines depict the breaking cases. The rate starting as high as it does in these examples, is clearly a result of the initial conditions used. In the absence of breaking, the circled curves would decay significantly and plateau at a very small value, somewhere less than  $0.05 \text{ m s}^{-1}$ . With breaking added the rate actually plateaus at a rate roughly twice as high (which value depends on the wind intensity). Hence, for the initial conditions chosen, the initial conditions largely control the rate of displacement, the Stokes drift is secondary in importance—note the diverging breaking and nonbreaking cases with Stokes drift (the intermediate pair of datasets). In the long-time limit, however, the breaking may overcome the Stokes drift velocity in affecting passive tracer transport. Since the breaking velocity terms in the momentum depend on the currents and the Stokes

drift, it is not possible to interpret, in general, whether the breaking velocity always suppresses transport or otherwise.

Figures 12b and 12d plot the 2 norm of the gradient of the vorticity, normalized by the norm of the vorticity itself, as a function of time. Again, case Fig. 12d corresponds to  $k_b$  amplitudes roughly 5-times larger, but otherwise the same as in Fig. 12b. The two thin upper curves correspond to the case in which the initial condition of the currents was zero (see Fig. 9). Whether the Stokes drift was present or not resulted in the comparable dispersion rates; the gradient and the vorticity norms are in equilibrium. For the case in which the breaking is not present, with nonzero Stokes drift, we obtain the circled line at the bottom (this is the dispersion associated with the flows depicted in Fig. 7). If the Stokes drift is not present the outcome is comparable. The dispersion again is nearly constant and thus the norms are approximately balancing, the norm of the field being dominant. Comparison of the jagged light lines and the circled one shows a difference that matches expectations: the breaking field makes the vorticity field uniformly rougher. Things are more interesting when we consider the dispersion associated with the flow depicted in Fig. 11. The lower light solid line corresponds to the no Stokes drift velocity case, and the other one to when the Stokes drift velocity is present. The dispersion curves are close to the nonbreaking case initially, then the trends become slightly different; however, whether

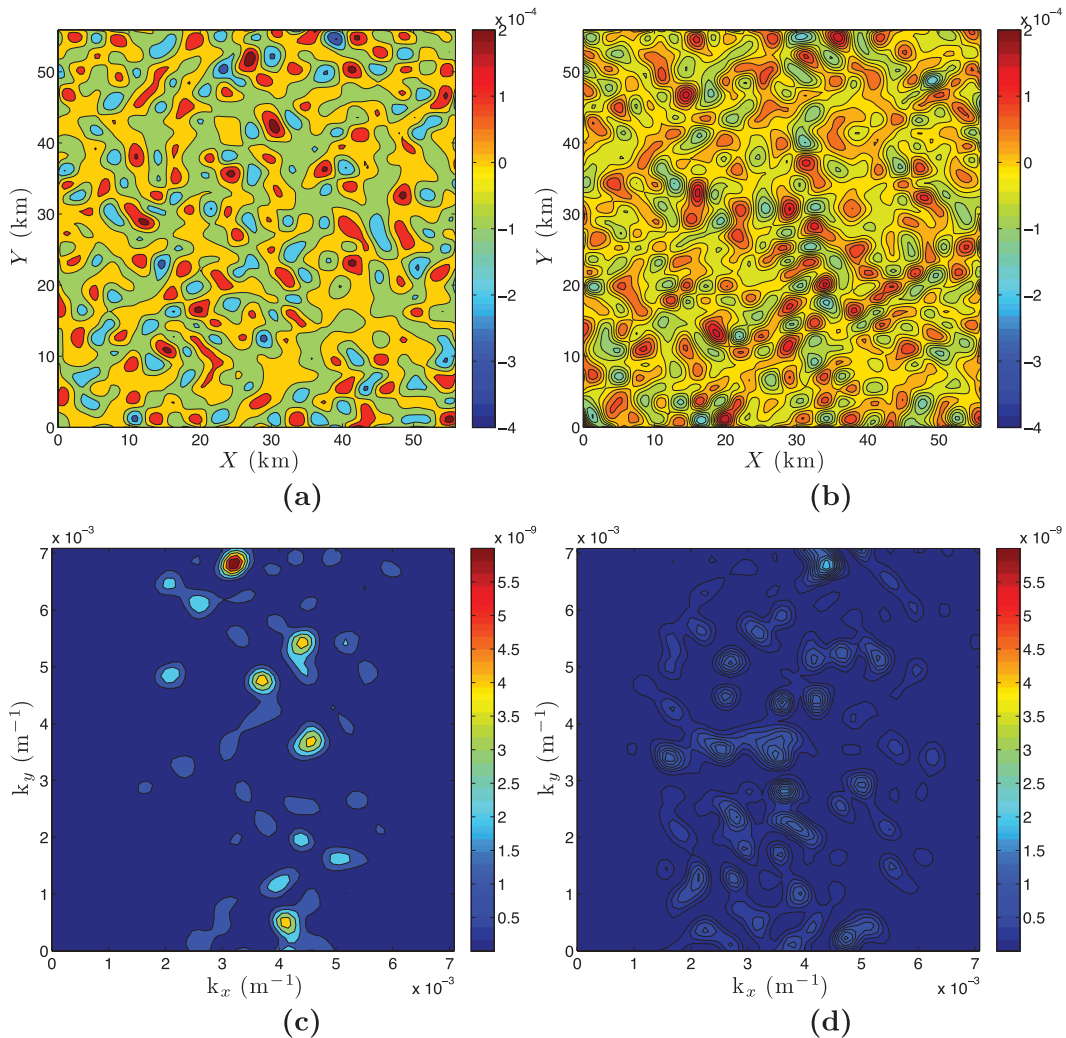


FIG. 9. Results after 12.8 h of simulation with an initially zero velocity field: (a),(c) vorticity  $Z^c(\mathbf{X})$  ( $\text{s}^{-1}$ ); (b),(d) spectrum ( $\text{m}^2 \text{s}^{-1}$ ) of vorticity. The first column, corresponds to the case  $\mathbf{u}^{\text{St}} = (0.259, 0) \text{ m s}^{-1}$ . The Stokes drift is zero in the second column. As in Fig. 8, but for the respective velocity fields. A comparison of (c) and (d) shows that the former is less spatially homogeneous and is the result of the presence of the drift velocity.

the Stokes drift velocity is present or otherwise, the dispersion asymptotes to the pure breaking case (the thin upper curves). The smooth dashed line in Fig. 12d is an exponential fit to these, with an exponent coefficient of 1. The exponential behavior is expected and results from the slow decay of the largest modes under the action of advection–diffusion.

## 5. Concluding remarks

In the model formulated here, whitecapping events affect currents in two ways: through breaking-generated momentum flux and breaking-generated diffusion. The breaking-generated momentum flux refers to modifications of the Reynolds stresses owing to the presence of

whitecapping. These affect momentum balances via the vortex force—the Bernoulli head. Breaking affects mass balance and tracer evolution, and it also affects the surface boundary conditions.

The breaking-generated momentum flux mechanism is arrived at by means of wave averaging and ensemble averaging the equations of motion and the boundary conditions, assuming that there is a separation of time scales and spatial scales for wave, current, and whitecapping velocities. The theoretical procedure is, in fact, the same as the one used to derive the three-dimensional and time-dependent large spatiotemporal-scale equations of motion for waves and currents and tracers, along with attendant boundary conditions (see McWilliams and Restrepo 1999).

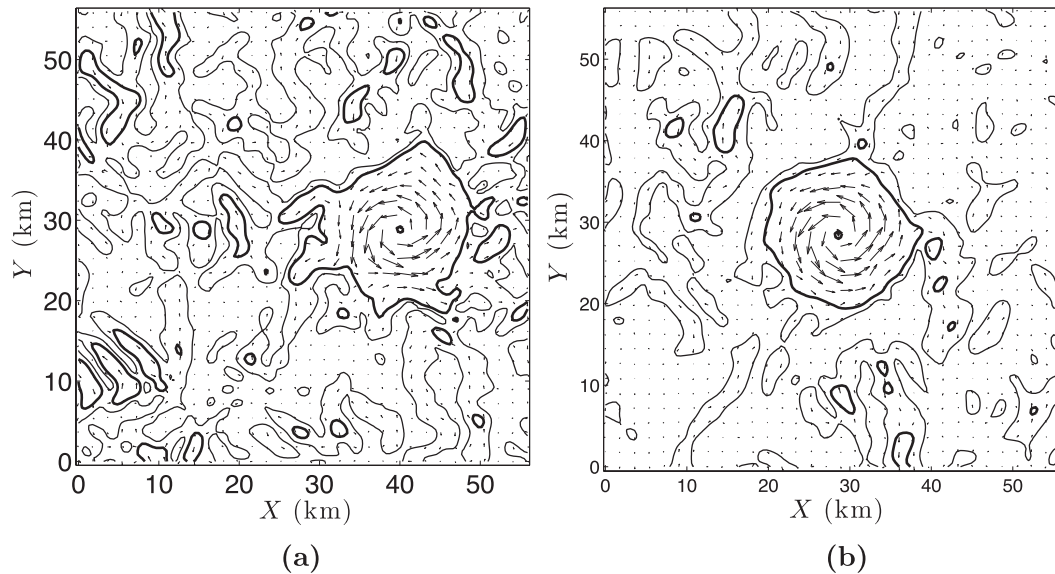


FIG. 10. Results after 12.8 h of simulation with the cyclonic initial condition as shown in Fig. 6. Velocity contours ( $\text{m s}^{-1}$ ): (a) the case  $\mathbf{u}^{\text{St}} = (0.259, 0) \text{ m s}^{-1}$  and (b) with the Stokes drift suppressed. Differences in the position of the cyclone are due to both the Stokes drift and the breaking field. Magnitude of the velocity contours at 0.05 (lighter) and 0.1  $\text{m s}^{-1}$  drawn.

The outcomes depend on how the velocity field is decomposed, here assumed to be in terms of a breaking velocity (which has very small time and length scales), an intermediate scale of waves and wave groups, and the larger spatiotemporal scales of currents. The assumption of an additive velocity field is motivated by the results in Restrepo (2007), where an analysis of the field showed that if the breaking velocity can be thought of as a process that affects the deterministic path diffusively, a multiplicative noise will mostly affect the waves, whereas additive noise would affect the currents.

The enhancement of diffusivity in the boundary layer due to a local thickening of the boundary layer caused by whitecapping activity is captured by the breaking-generated diffusion. This enhanced diffusivity affects currents and tracers. This effect is modeled here in a manner similar to the way that is proposed by Sullivan et al. (2007): it is parameterized as an eddy diffusivity whose strength depends on the amplitude of the wave groups. The eddy diffusivity, however, is triggered by breaking events, whose location in space–time, in the absence of any other dynamic effects, follow a Poisson distribution. The enhancement of the mixed layer due to whitecapping, captured here by a  $k$ – $\epsilon$  model for diffusion, could likely be replaced by a more appropriate model if the boundary layer itself was resolved and considered in detail. Nevertheless, for the scales of interest to us, namely, the current scales, the upscaling of the boundary layer effects will produce a model similar to the one adopted. However, the dependence on wave

and group dynamics would likely improve by a careful consideration of the boundary layer itself.

Example calculations showed that the presence of breaking events roughened the velocity and vorticity fields. It is possible, from the fields themselves or their spectra, to see in what direction the constant wind was blowing that created the white caps in the first place. The spectrum evolves in time; however, this is mostly the result of the random phase assumption of the waves composing the groups. The advection of vorticity was mainly controlled by the Stokes drift velocity, at least for the wind speeds chosen here. When comparing cases with and without breaking and tracking the peak vorticity we found, however, that breaking could modify the advection of vorticity in surprising ways. The rate of dispersion was found to be controlled by the breaking waves, in the long-time limit. If there was greater interaction between the waves and the currents, as would be the case in the shallow-water limit (cf. McWilliams et al. 2004), breaking effects would induce breaking momentum flux, changes in the wave refraction via the currents, and in turn these would affect the vortex force and the Bernoulli head.

It should be emphasized that the results we presented here are generally applicable to a large basin, in three space dimensions and time. The feedback from the currents to the waves, and to the breaking field, is absent in this presentation because of our choice of the wave–current interaction framework—that is, the use of the basin-scale model in McWilliams and Restrepo (1999)

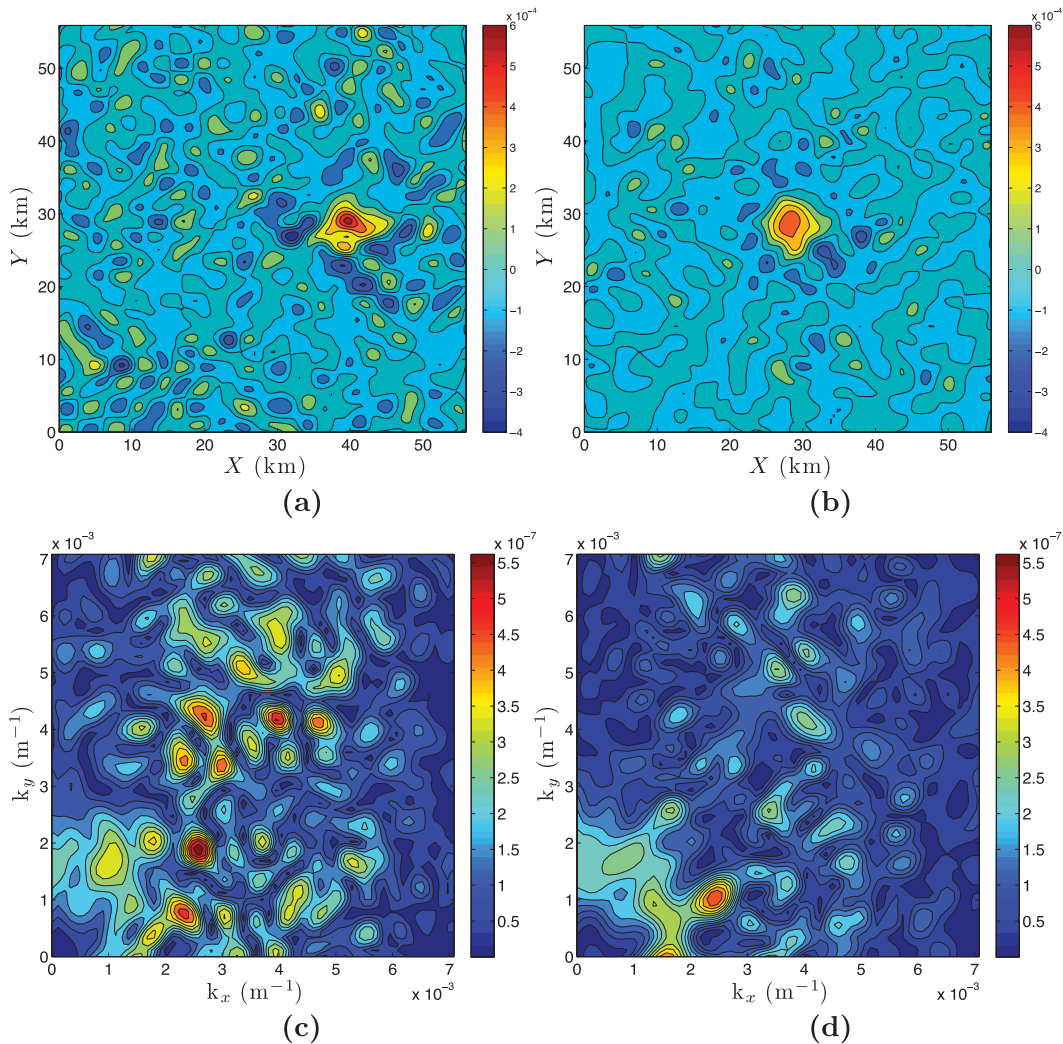


FIG. 11. Results after 12.8 h of simulation with the cyclonic initial condition as shown in Fig. 6. (a),(d) Velocity contours ( $\text{m s}^{-1}$ ) are shown. (a),(b) Vorticity  $Z^c(\mathbf{X})$  ( $\text{s}^{-1}$ ) and (c),(d) spectrum ( $\text{m}^2 \text{s}^{-1}$ ) of vorticity. (a),(c) correspond to the case  $\mathbf{u}^{\text{St}} = (0.259, 0) \text{ m s}^{-1}$ . In (b),(d) the Stokes drift is zero. The spectrum of the cyclone is less evident in (c) than in (d). See Fig. 10 for corresponding velocity fields.

as opposed to the more complete model in McWilliams et al. (2004) (the specific wave–current interactions are a result of the asymptotic balances). Revisiting the derivation presented here using the shelf model used in McWilliams et al. (2004) will determine how the effects on the currents will then feedback onto the large-scale variation of the waves. Furthermore, the effect of breaking events on the vertical transport of stresses, an effect that could be surmised as being significant from Fig. 1, was not explored in the example calculation chosen here.

Our model requires a parameterization of the breaking velocity itself. This could be obtained, in principle, from observational data. Here, we proposed a parameterization for the breaking velocity, endowed with

empirical rules that are based upon a priori knowledge of certain ubiquitous characteristics of wave breaking. We adopt an empirically derived analytical representation of the breaking events to make the breaking velocity explicit; however, the form of these is not crucial at the scales we are interested in as these events happen at very small spatiotemporal scales, compared to those of interest. We incorporate a spatiotemporal and energetic rule about energy convergence within nonlinear wave groups to predict the onset of wave breaking (or more specifically whitecapping) in the oceanic domain; this rule has been confirmed for unidirectional waves in wave tank experiments. We built the statistical distribution of wave-breaking strength and scale upon the representation of deep gravity waves by Gaussian

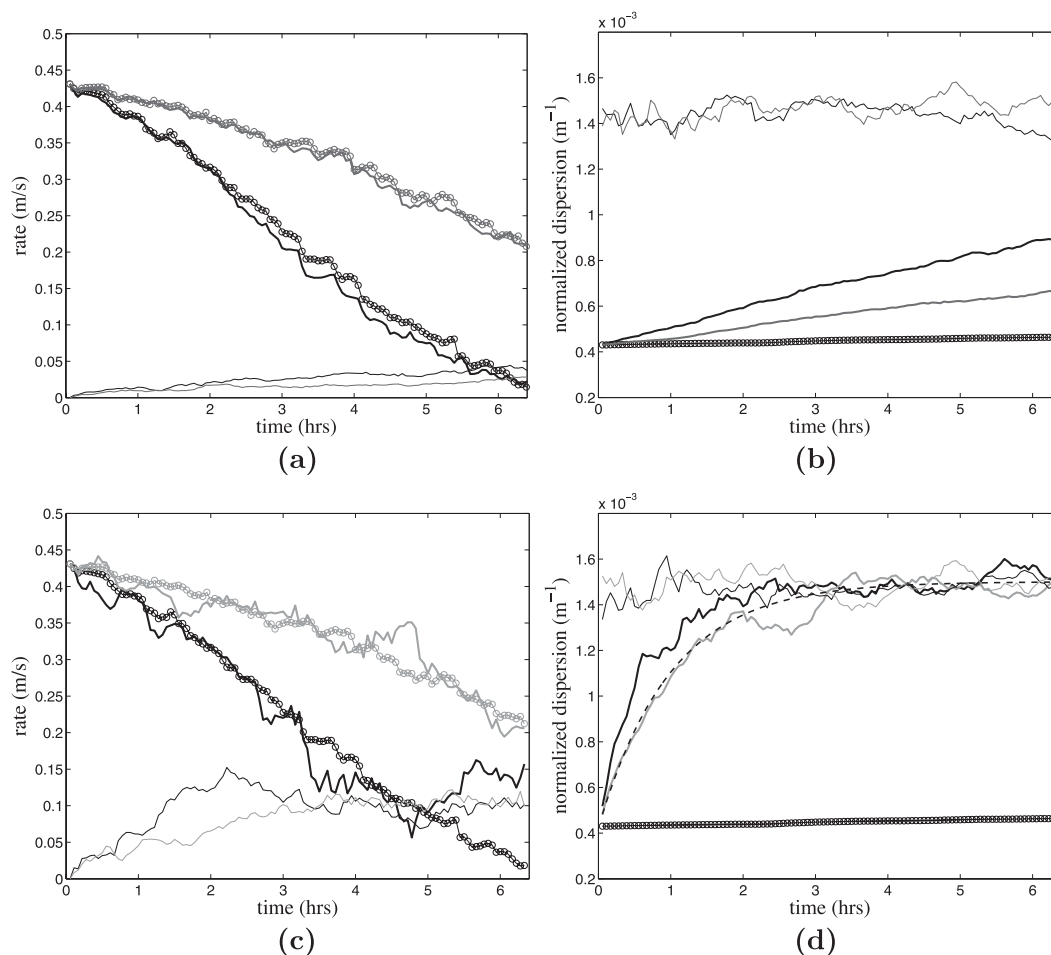


FIG. 12. (a) Average rate of motion of a collection of 32 particles, placed initially at a radius of 5 km from the center of the cyclone. (b) 2 norm of the gradient of the vorticity, normalized by the norm of the vorticity itself. Light lines, no Stokes drift; dark lines, with Stokes drift  $\mathbf{u}^{\text{St}} = (0.259, 0) \text{ m s}^{-1}$ . Lines with circles correspond to no breaking, solid heavy lines correspond to breaking cases. Thin lines correspond to zero initial conditions on the currents, all others correspond to the cyclonic initial condition shown in Fig. 6. Both figures highlight the fact that dispersive effects are mostly controlled by the breaking field, when present. (b) It is shown that the dispersion asymptotes to the pure breaking case, whether the Stokes drift velocity is present or not. The dispersion is smallest when no breaking is invoked. (c),(d) The average rate of motion and 2 norm of the gradient, with all conditions the same except that the overall magnitude of  $k_b$  was forced to be 5 times greater than in the counterparts (a),(b). Dashed line in (d) is an exponential fit in time.

surfaces, therefore establishing a modeling bridge between the physics of breaking events, wind conditions, and sea age for large scales.

Furthermore, faced with the lack of large-scale oceanic wave-breaking data for different sea ages, we proposed a methodology to generate random wave-breaking events under the assumption of a Gaussian sea surface of fixed energy spectrum. This methodology is new, as far as we can tell, and its outcomes are easily testable should large-scale breaking data become available. The main advantage of our approach lies in that it combines in a straightforward fashion the well-established Gaussian process model for the ocean surface with recent

developments in the diagnosis and dynamics of wave-breaking events—namely, the use of the wave group energy convergence rate as a breaking threshold (Banner and Peirson 2007; Song and Banner 2002) and the characterization of the momentum in laboratory-scale wave-breaking events (see Sullivan et al. 2004). To make this methodology practical, we extended the techniques of wave group detection and wave group analysis, pioneered by Longuet-Higgins (1984) and further developed by Song and Banner (2002), to the case of random surfaces in two dimensions. In doing so, we proposed the mean Euler characteristic as a useful parameter in the identification of wave groups in random wave fields.

The net result of our methodology is that it allowed us to treat the statistical parameterization and energetic estimates of wave breaking as outcomes of the model, not imposed constraints.

The algorithm for the detection and tracking of wave groups produces two main outcomes: the intensity measure of a Poisson-point process with space–time locations of wave-breaking events and the joint distribution of the strength and wavenumber of breaking waves (see Fig. 4). The results are qualitatively compatible with observations. First, the obtained wave groups are uniformly distributed in space–time and span 2–3 mean spatial wave periods—their estimated mean energy and convergence rate having values within the observed ranges in laboratory experiments. Second, the scale of wave-breaking events was predicted near the dominant wavenumber and of a strength in concordance with numerical and experimental results reported in the literature reviewed above. Finally, the underlying assumption of a Poisson process for the space–time location of breaking events, being consistent with the statistical homogeneity of a Gaussian ocean surface, was tested via simulations (see Fig. 5).

*Acknowledgments.* This research is supported by the National Science Foundation through the Grant DMS0335360. JMR thanks the Institute of Mathematics and its Applications, where some of the work was done. We thank Brad Weir for his comments and suggestions on the manuscript presentation.

#### REFERENCES

- Adler, R. J., 1978: On the envelope of a Gaussian random field. *J. Appl. Probab.*, **15**, 502–513.
- , and J. E. Taylor, 2007: *Random Fields and Geometry*. Springer Monogr., No. XVIII, Springer, 448 pp.
- Alves, J., and M. L. Banner, 2003: Performance of a saturation-based dissipation-rate source term in modeling the fetch-limited evolution of wind waves. *J. Phys. Oceanogr.*, **33**, 1274–1298.
- Banner, M. L., and D. H. Peregrine, 1993: Wave breaking in deep water. *Annu. Rev. Fluid Mech.*, **25**, 373–397.
- , and W. L. Peirson, 2007: Wave breaking onset and strength for two-dimensional deep-water wave groups. *J. Fluid Mech.*, **585**, 93–115.
- Bauer, E., and Coauthors, 1988: The WAM Model—A third generation ocean wave prediction model. *J. Phys. Oceanogr.*, **18**, 1775–1810.
- Burchard, H., 2001: Simulating the wave-enhanced layer under breaking surface waves with two-equation turbulence models. *J. Phys. Oceanogr.*, **31**, 3133–3145.
- Craig, P. D., and M. L. Banner, 1994: Modeling wave-enhanced turbulence in the ocean surface layer. *J. Phys. Oceanogr.*, **24**, 2546–2559.
- Craik, A. D. D., and S. Leibovich, 1976: A rational model for Langmuir circulations. *J. Fluid Mech.*, **73**, 401–426.
- D’Asaro, E. A., 2001: Turbulent vertical kinetic energy in the ocean mixed layer. *J. Phys. Oceanogr.*, **31**, 3530–3537.
- Donelan, M. A., 1982: The dependence of the aerodynamic drag coefficient on wave parameters. *Proc. First Int. Conf. on Meteorological and Air–Sea Interaction of the Coastal Zone*, The Hague, Netherlands, Amer. Meteor. Soc., 381–387.
- Elfouhaily, T., B. Chapron, K. Katsaros, and D. Vandemark, 1997: A unified directional spectrum for long and short wind-driven waves. *J. Geophys. Res.*, **102**, 781–815.
- Ferziger, J. H., and M. Peric, 1997: *Computational Methods for Fluid Dynamics*. Springer Verlag, 364 pp.
- Gemmrich, J., and D. Farmer, 2004: Near-surface turbulence in the presence of breaking waves. *J. Phys. Oceanogr.*, **34**, 1067–1086.
- Huang, H. E., 1979: On surface drift currents in the ocean. *J. Fluid Mech.*, **91**, 191–208.
- Illian, J., A. Penttinen, H. Stoyan, and D. Stoyan, 2008: *Statistical Analysis and Modelling of Spatial Point Patterns: Statistics in Practice*. John Wiley & Sons, 534 pp.
- Komen, G. J., L. Cavaleri, M. Donelan, K. Hasselmann, and S. Hasselmann, 1994: *Dynamics and Modelling of Ocean Waves*. Cambridge University Press, 532 pp.
- Lane, E. M., J. M. Restrepo, and J. C. McWilliams, 2007: Wave–current interaction: A comparison of radiation-stress and vortex-force representations. *J. Phys. Oceanogr.*, **37**, 1122–1141.
- Longuet-Higgins, M. S., 1984: Statistical properties of wave groups in a random sea state. *Philos. Trans. Roy. Soc. London*, **A312**, 219–250.
- McWilliams, J. C., and J. M. Restrepo, 1999: The wave-driven ocean circulation. *J. Phys. Oceanogr.*, **29**, 2523–2540.
- , —, and E. M. Lane, 2004: An asymptotic theory for the interaction of waves and currents in coastal waters. *J. Fluid Mech.*, **511**, 135–178.
- Melson, A., 1996: Effects of wave breaking on the surface drift. *J. Geophys. Res.*, **101**, 12 071–12 078.
- Melville, W. K., 1996: The role of surface-wave breaking in air–sea interaction. *Annu. Rev. Fluid Mech.*, **28**, 279–321.
- Niedermeier, A., J. Borge, S. Lehner, and J. Schultz-Stellenfleth, 2005: A wavelet-based algorithm to estimate ocean wave group parameters from radar images. *IEEE Trans. Geosci. Remote Sens.*, **43**, 327–336.
- Phillips, O. M., and M. L. Banner, 1974: Wave breaking in the presence of wind drift and swell. *J. Fluid Mech.*, **66**, 625–640.
- Restrepo, J. M., 2007: Wave breaking dissipation in the wave-driven ocean circulation. *J. Phys. Oceanogr.*, **37**, 1749–1763.
- Song, J.-B., and M. L. Banner, 2002: On determining the onset and strength of breaking for deep water waves. Part I: Unforced irrotational wave groups. *J. Phys. Oceanogr.*, **32**, 2541–2558.
- Sullivan, P. P., J. C. McWilliams, and W. K. Melville, 2004: The oceanic boundary layer driven by wave breaking with stochastic variability. I: Direct numerical simulation of neutrally-stratified shear flow. *J. Fluid Mech.*, **507**, 143–174.
- , —, and —, 2007: Surface gravity wave effects in the oceanic boundary layer: Large-eddy simulation with vortex force and stochastic breakers. *J. Fluid Mech.*, **593**, 405–452.
- Terray, E., M. Donelan, and Y. Agrawal, 1996: Estimates of kinetic energy dissipation under breaking waves. *J. Phys. Oceanogr.*, **26**, 792–807.
- Tian, Z., M. Perlin, and W. Choi, 2008: Evaluation of a deep-water wave breaking criterion. *Phys. Fluids*, **20**, 066604–066604-13.
- Warner, C. D., and M. E. McIntyre, 1999: Toward an ultra-simple spectral gravity wave parameterization. *Earth Planets Space*, **51**, 475–484.